

1 **Nematode Extracellular Protein Interactome Expands Connections between Signaling**  
2 **Pathways**

3 Wioletta I. Nawrocka,<sup>1,2,3,\*</sup> Shouqiang Cheng,<sup>1,2,3,\*</sup> Bingjie Hao,<sup>4,\*</sup> Matthew C. Rosen,<sup>1,2,3</sup> Elena  
4 Cortés,<sup>1,2,3</sup> Elana E. Baltrusaitis,<sup>1,2,3</sup> Zainab Aziz,<sup>1,2,3</sup> István A. Kovács,<sup>4,5,6</sup> Engin Özkan<sup>1,2,3,†</sup>

5 <sup>1</sup> Department of Biochemistry and Molecular Biology, <sup>2</sup> Institute for Neuroscience, and <sup>3</sup> Institute  
6 for Biophysical Dynamics, The University of Chicago, Chicago, IL 60637, USA.

7 <sup>4</sup> Department of Physics and Astronomy, <sup>5</sup> Northwestern Institute on Complex Systems, and <sup>6</sup>  
8 Department of Engineering Sciences and Applied Mathematics, Northwestern University,  
9 Evanston, IL 60208, USA.

10 \* equal contribution

11 † contact: eozkan@uchicago.edu

12

13 **ABSTRACT**

14 Multicellularity was accompanied by the emergence of new classes of cell surface and secreted  
15 proteins. The nematode *C. elegans* is a favorable model to study cell surface interactomes, given  
16 its well-defined and stereotyped cell types and intercellular contacts. Here we report our  
17 *C. elegans* extracellular interactome dataset, the largest yet for an invertebrate. Most of these  
18 interactions were unknown, despite recent datasets for flies and humans, as our collection  
19 contains a larger selection of protein families. We uncover new interactions for all four major axon  
20 guidance pathways, including ectodomain interactions between three of the pathways. We  
21 demonstrate that a protein family known to maintain axon locations are secreted receptors for  
22 insulins. We reveal novel interactions of cystine-knot proteins with putative signaling receptors,  
23 which may extend the study of neurotrophins and growth-factor-mediated functions to nematodes.  
24 Finally, our dataset provides insights into human disease mechanisms and how extracellular  
25 interactions may help establish connectomes.

26

27 **Keywords:** Protein-protein interactions; Extracellular space; Cell surface receptor; Secreted  
28 protein; High-throughput interaction assay; *Caenorhabditis elegans*

## 29 INTRODUCTION

30 Cell surface receptors and secreted ligands build structures connecting cells, mediate  
31 communications between cells, sense and respond to extracellular cues, and function as  
32 molecular tags to identify cellular populations. These proteins include cell adhesion molecules,  
33 signaling receptors, cytokines, growth factors, and secreted cues for cellular migration among  
34 others, which are essential for most multicellular life.<sup>1</sup> However, much of the extracellular  
35 proteome remains without known binding partners, which is a roadblock for revealing the various  
36 functional roles of cell surface and secreted proteins in multicellular systems. Since membrane  
37 proteins and cell surface receptors constitute the majority of targets for current therapies and are  
38 more readily accessible to new therapies,<sup>2</sup> extracellular interactions are important for  
39 understanding the mode-of-action of existing therapies, as well as developing new ones.

40 Recent expansions of genomic sequence data and bioinformatics tools to recognize cell surface  
41 and secreted proteins have opened the study of extracellular interactions to specialized high-  
42 throughput methods.<sup>3-5</sup> One of the most effective approaches has been secreted bait/prey capture  
43 strategies that use recombinantly expressed ectodomain libraries where bait and prey have been  
44 oligomerized, resulting in significant increase in effective affinity for the bait-prey pair. Such  
45 avidity-enhanced assays have been instrumental in the discovery of interactions controlling cell-  
46 cell recognition for synapse targeting and avoidance,<sup>4,5</sup> neuronal repulsion,<sup>6</sup> and regulatory  
47 signaling networks in plant growth and immunity,<sup>7</sup> among others.

48 Despite these improvements, several issues with extracellular interactome studies remain: First,  
49 the existing studies have focused on an important but limited set of protein families, including the  
50 immunoglobulin (IG) superfamily<sup>3,4,8-10</sup> and proteins with leucine-rich repeat (LRR) domains,<sup>4,7,11</sup>  
51 while most of the known fold space in the extracellular milieu has been ignored. Second, there is  
52 a need for throughput improvements to allow for expansion of datasets towards the full  
53 interactome of cell surface and secreted proteomes. Finally, the application of the methodology  
54 to important model organisms lags. Animal genomes contain groups of conserved cell surface  
55 receptors and ligands with related functions throughout many taxa, as well as specific classes of  
56 proteins to mediate functions within few taxa or proteins with different binding partners in different  
57 taxa. The challenge of predicting whether a given set of molecular interactions are preserved

58 across many species is a significant barrier to incorporating knowledge generated across model  
59 organisms.

60 The nematode *Caenorhabditis elegans* has been a pioneering model organism for studying  
61 embryogenesis, nervous system development, behavior, aging and many other aspects of  
62 biology.<sup>12</sup> The *C. elegans* genome contains a smaller number of paralogs for cell surface protein  
63 families shared across bilaterians,<sup>13</sup> which makes it easier to cover a larger group of receptor and  
64 ligand families relevant for human physiology. In this study, we increased the throughput of our  
65 previous avidity-based interaction screen strategy and applied it to a collection of 379 *C. elegans*  
66 ectodomains, for a putative interaction space of 72,010 possible interactions, covering 12 domain  
67 families in full and 74 domain families in part, nearly all with representation in the human genome  
68 (**Table S1**). Using a statistical method we developed for data analysis, we report 185 interactions  
69 at our intermediate confidence level, including 159 (86%) previously unknown or unpredicted by  
70 homology to known complexes. Here, we highlight and validate novel interactions between axon  
71 guidance cues and ligands from separate pathways, insulin interactions with a class of secreted  
72 IG domain proteins, and differences in interactions between mammalian and nematode orthologs.  
73 We further reveal complexes of secreted proteins of growth factor folds with their signaling  
74 receptors, and compare them to mammalian counterparts, including a novel pair with connections  
75 to human disease. Finally, we discuss interactions likely to be important in the synaptic wiring of  
76 the nervous system.

## 77 **RESULTS**

### 78 **Ectodomain Library**

79 While classical high-throughput interaction discovery technologies have proven to be highly  
80 effective for many protein classes, these strategies have remained ineffective for studying  
81 membrane proteins, cell surface receptors and secreted proteins,<sup>14</sup> which make up a large fraction  
82 of animal proteomes (**Figure S1A**). Published extracellular interactome studies have focused on  
83 IG, FN (Fibronectin-type III) and LRR domains, which are some of the largest protein families in  
84 the human proteome,<sup>3,4,7-9,11</sup> but have ignored the rest. To address the knowledge gap in the  
85 extracellular interactomes, we chose to study the *C. elegans* proteome (**Figure S1A**), which have

86 smaller IG, FN, and LRR families compared to mammalian proteomes (e.g., ~600 IG proteins in  
87 humans vs. ~70 in *C. elegans*),<sup>15,16</sup> allowing us to include other domain families, covering a more  
88 diverse selection of protein fold and function space with our high-throughput assay. Here, we  
89 subcloned nearly all ectodomains containing IG, FN, LRR, Cadherin (Cad), Epidermal growth  
90 factor (EGF), CUB, Laminin-N (LamN), Thrombospondin type-I (TSP1), Integrin, GAIN, Cystine-  
91 knot cytokine, and ADAM-type Cys-rich domains, as well as domain families found in known axon  
92 guidance cues and receptors (**Figures 1A-1C, Table S1**). Our ectodomain collection also  
93 includes some, but not all, ectodomains with Furin, Insulin, Kazal, Kunitz, LDLa, LY, SEA,  
94 Sushi/CCP, von Willebrand Factor type A, C and D (VWA, VWC, VWD), and WAP domains  
95 among others. Our diverse collection comprises expression constructs of 379 unique ectodomain  
96 variants, from 374 cell surface receptor and secreted protein genes with ~86 types of domains or  
97 folds, cloned in both bait and prey expression plasmids for interaction screening, ranging from 57  
98 to 3,220 amino acids (average: 672 amino acids), not including the tags in bait and prey  
99 expression constructs. 43% of the ectodomain library are from secreted proteins, while the rest  
100 are predicted to be cell surface receptors anchored by transmembrane helices or  
101 glycosylphosphatidylinositol (GPI) anchors (**Figure 1A**).

## 102 **Assay Development**

103 The Extracellular Interactome Assay (ECIA) uses Fc-tagged secreted ectodomains as bait  
104 captured on Protein A-coated plates, and Alkaline phosphatase-tagged ectodomains as prey for  
105 the detection of binding to the immobilized bait (**Figures 1D and E**). Essential to the sensitivity of  
106 the assay is the pentameric coiled coil included in the prey constructs, which increases effective  
107 affinity up to 10,000-fold through avidity,<sup>4</sup> as previously implemented in similar strategies.<sup>3,5</sup>

108 The first generation of the ECIA methodology used the inducible metallothionein promoter for  
109 protein expression in the *Drosophila* S2 cell line. For this study of the *C. elegans* interactome, we  
110 continued to use the well-established S2 line, as insects are phylogenetically closer to nematodes  
111 when compared to other sources of established protein expression lines. However, we  
112 implemented several changes to simplify our protocols and improve throughput. First, we modified  
113 our expression plasmids to use the constitutively active Actin 5C promoter, which removed the  
114 induction step during expression, while improving expression levels as we observed (**Figures**



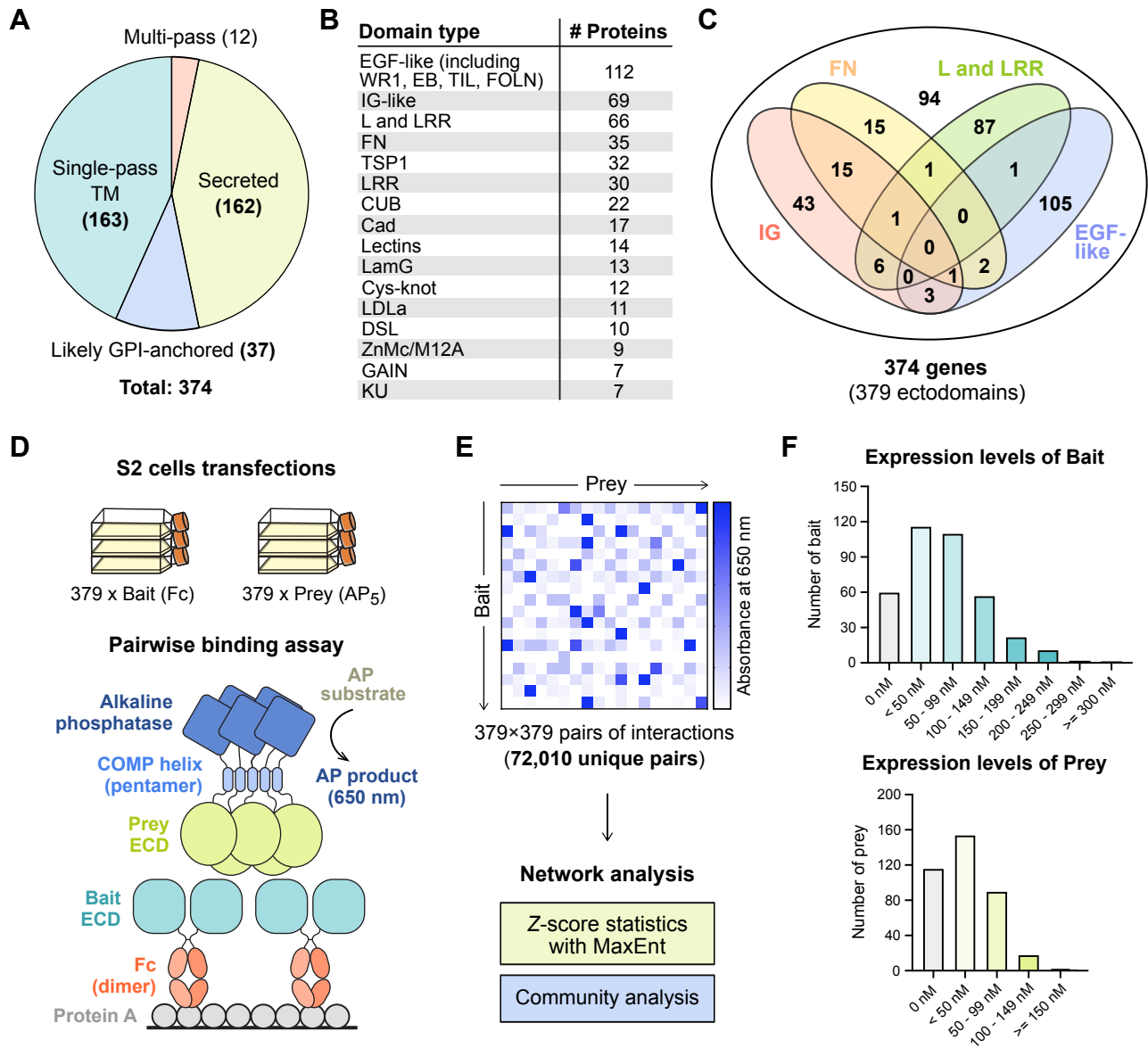


**Figure 1.** The *C. elegans* ectodomain collection and high-throughput interaction assay design.

**A.** The distribution of secreted and membrane-anchored proteins in our *C. elegans* ectodomain collection.

**B, C.** The distribution of protein domains in the ectodomain collection.

**D, E.** The design of the ECIA pipeline and data analysis.

**F.** The expression levels of bait and prey proteins in the S2 cell culture media.

115 **S1B-E)** and as previously reported for other proteins in low-throughput studies.<sup>17,18</sup> We also  
116 implemented the use of 384-well plates and robotics to decrease transfection volumes, speed up  
117 the interaction assay, and decrease cost. Lastly, the advent of Gibson assembly protocols for  
118 subcloning allowed us to simplify our previous cloning strategy of Topo TA cloning followed by  
119 Gateway recombination. We cloned 63 ectodomain open-reading frames using existing cDNAs in  
120 a *C. elegans* ORF Clone Collection (GE Healthcare), 16 from our laboratories' collections, 9 using  
121 RT-PCR from a mixed *C. elegans* mRNA library, and corrected any mutation(s) and/or intron(s)  
122 likely introduced during RT-PCR. We had the remaining 288 ORFs synthesized, choosing the  
123 longest splice variant whenever possible and practical. As we kept the Gateway recombination  
124 sequences intact in our plasmids, our ectodomain cDNA collection can be easily re-purposed for  
125 other formats and assays. Despite the improvements, 23% of our constructs did not yield  
126 detectable expression and secretion, as judged by western blotting of conditioned media (**Figure**  
127 **1F**). The median concentrations in the media were estimated to be 57 nM for bait and 17 nM for  
128 prey constructs.

## 129 **Analysis of ECIA Results**

130 ECIA reports interactions by measuring absorbance from the product of the alkaline phosphatase  
131 reaction. To detect significant interactions, we have previously calculated z-scores using trimmed  
132 mean and standard deviation values for each bait, and then used these normalized values to  
133 calculate z-scores across each prey.<sup>4</sup> To improve our detection of significant hits here, we utilized  
134 a maximum entropy network ensemble-based technique<sup>19</sup> to construct a statistical model that  
135 captures the absorbance background. Significant interactions are identified by comparing the  
136 observations with the modeled background (see Methods and **Figure S2** for details) using z-  
137 scores, where the standard deviation quantifies systematic errors. As true PPIs are likely to be  
138 detectable regardless of whether a protein is the bait or prey, we symmetrize the z-scores as  $z =$   
139  $\frac{z_{A \rightarrow B} + z_{B \rightarrow A}}{\sqrt{2}}$  (**Table S2**). This approach yields one continuous-valued weight/score for the interaction  
140 between each pair of proteins. Using absorbance values collected at 2 hours following application  
141 of the AP substrate, an intermediate score threshold of  $z_{min} = 8.4$  yields a protein-protein  
142 interaction graph with 185 interactions ( $z > z_{min}$ ) (**Figures S2D, S2E** and **Table S3**). These  
143 interactions align strongly with those identified using our previously employed scoring approach

144 (Table S3), but with a more rigorous standard in selecting the threshold. Lower values of  $z_{min}$   
145 correspond with more liberal criteria for determining which interactions to include, and thus  
146 networks with more edges.

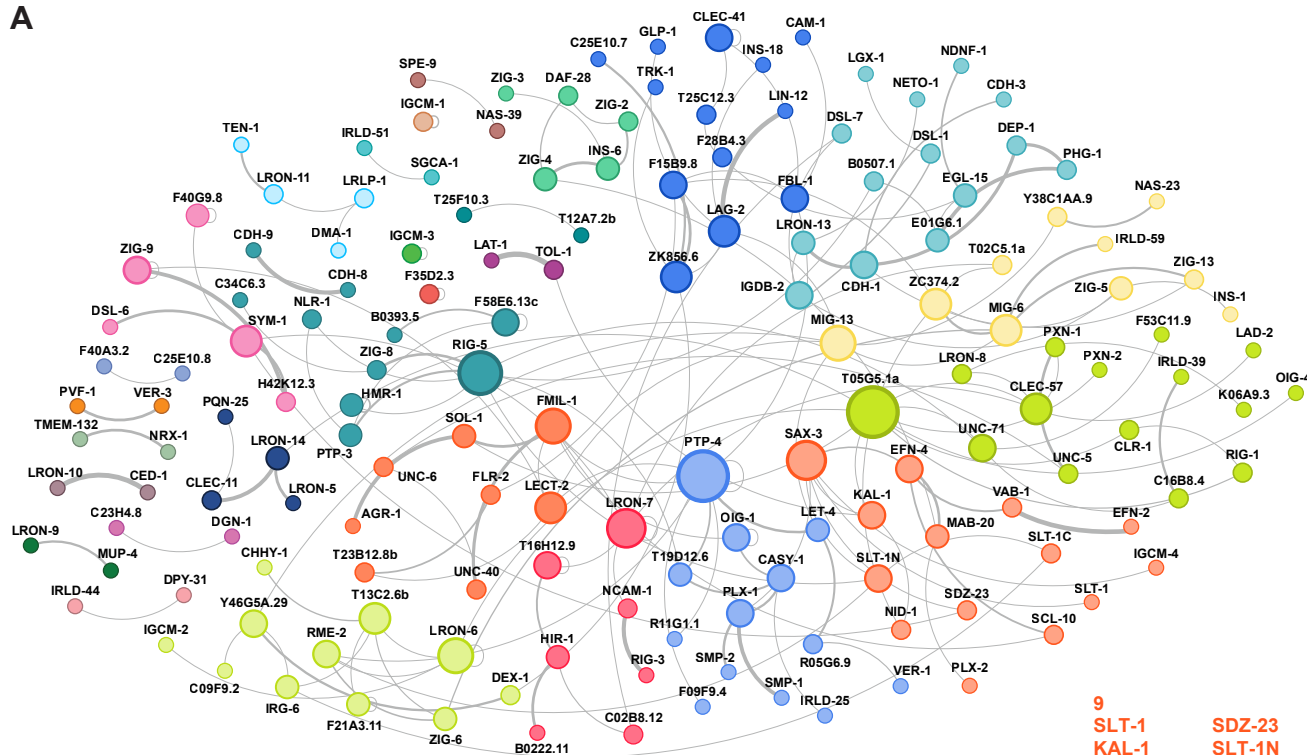
## 147 Community Analysis of ECIA Interaction Networks

148 Although protein-protein interaction networks are built from pairwise measurements, they often  
149 also reflect higher-order, functionally-relevant relationships between groups of proteins. One  
150 particularly successful approach for identifying higher-order relationships is community  
151 detection,<sup>20</sup> which seeks to identify ‘insular’ subgroups of proteins – where connections between  
152 pairs of proteins within the group are stronger than those made with proteins outside the group.  
153 The interactions within these groups can reflect the sharing of latent relationships even between  
154 pairs of proteins that do not themselves directly interact. We applied a modularity optimization  
155 method to the ECIA interaction network to investigate its community structure.<sup>21</sup> As expected,  
156 communities tend to group proteins with known functions (Figure 2). For example, proteins known  
157 to mediate axon guidance, those belonging to Robo, Slit, Ephrin and Eph, and one of the  
158 Semaphorins and Plexins, belong to the same community (community 9 in Fig. 2), while the  
159 remaining Semaphorins and Plexin are in the same community with an RPTP (PTP-4), VER-  
160 1/VEGFR, and Calsyntenin (CASY-1), proteins with known functions in regulating axon guidance  
161 (community 11 in Fig. 2).<sup>22,23</sup> To capture functional groupings among a larger subset of the  
162 network (beyond the intermediate thresholds described above), we conducted the same analysis  
163 across 20-fold variation in  $z_{min}$ , from conservative ( $z_{min} = 40$ ,  $N = 60$  interactions) to liberal  
164 ( $z_{min} = 2$ ,  $N = 654$  interactions). Using the communities calculated over this range of thresholds,  
165 we found nodes that repeatedly belonged to the same community. For every protein  $P$  for which  
166 we observed an interaction, we report (a) the full set of proteins partitioned into the same  
167 community as  $P$  for any tested  $z_{min}$ , and (b)  $P$ 's “canonical neighbors”, the subset of proteins that  
168 belong to the same community as  $P$  across different choices for  $z_{min}$  (Table S4).

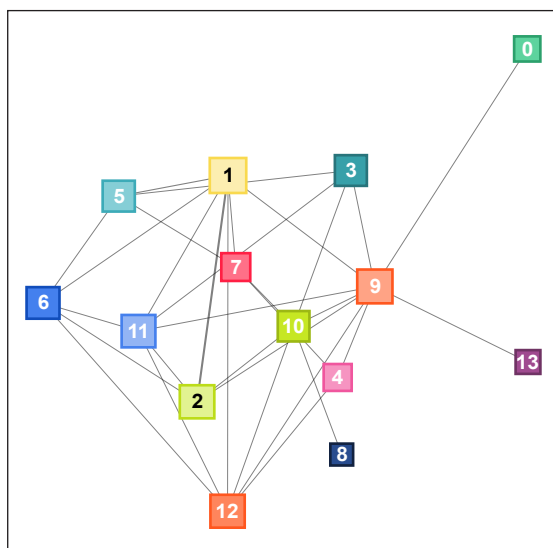
## 169 Higher-order axon guidance complexes

170 One of the highly conserved processes in nervous system development is the control of the  
171 direction of axonal growth by interactions of guidance cues with their neuronal receptors. Our

**A**



**B**



**C**

0	ZIG-2 ZIG-4 INS-6	ZIG-3 DAF-28	5	B0507.1 IGDB-2 DSL-7 EGL-15 LGX-1 CDH-3 NETO-1	9	SLT-1 KAL-1 SLT-1C NID-1 IGCM-4 EFN-2 PLX-2
1	ZIG-5 MIG-6 ZIG-13 INS-1 MIG-13	IRLD-59 NAS-23 Y38C1AA.9 ZC374.2 T02C5.1a	6	C25E10.7 LAG-2 CAM-1 TRK-1 FBL-1 F28B4.3 INS-18	10	PXN-2 LRON-8 UNC-5 F53C11.9 IRLD-39 RIG-1 T05G5.1a LAD-2 CLEC-57
2	ZIG-6 DEX-1 LRON-6 RME-2 CHHY-1 IRG-6	C09F9.2 F21A3.11 IGCM-2 T13C2.6b Y46G5A.29	7	RIG-3 C02B8.12 NCAM-1 T16H12.9	11	IRLD-25 OIG-1 F09F9.4 R05G6.9 VER-1 SMP-2 PLX-1
3	ZIG-8 B0393.5 RIG-5 F58E6.13c	C34C6.3 PTP-3 NLR-1 HMR-1	8	LRON-5 PQN-25	12	UNC-6 UNC-40 FML-1 FLR-2
4	ZIG-9 SYM-1 H42K12.3	DSL-6 F40G9.8	13	LAT-1	13	SDZ-23 SLT-1N SCL-10 VAB-1 SAX-3 EFN-4 MAB-20

**Figure 2.** Interactions and the community structure of the extracellular interaction.

**A.** Network of moderate-confidence ( $z_{\min} > 8.4$ ) protein-protein interactions ( $N = 185$ ) identified via the maximum-entropy method; proteins are colored by community grouping.

**B.** Network of community-community interactions. Only *connected communities* (communities with at least one protein making at least one interaction outside the community;  $N = 14$ ) are shown.

**C.** List of proteins in each connected community.

172 study included the known cue-receptor pairs from the four classical guidance systems: Slit and  
173 Robo, Ephrins and Ephs, Semaphorins and Plexins, and Netrin (UNC-6) and its receptors, UNC-  
174 40/DCC and UNC-5.<sup>24</sup> To our surprise, we observed novel interactions with high confidence that  
175 connected the three axes in the extracellular space (**Figure 3A and Table S3**). SAX-3/Robo  
176 interacts with its classical ligand SLT-1 and its N-terminal processed fragment (SLT-1N), but also  
177 with the Ephrin EFN-4 and Plexin PLX-1. This connects the Robo signaling axis to receptors of  
178 both the Ephrin and Plexin axes. In addition, EFN-4 interacts with the Semaphorin MAB-20,  
179 physically connecting Ephrin receptor with a Plexin ligand in the extracellular space. We  
180 successfully replicated these results and others involving guidance receptors and cues using  
181 ECIA (**Figures 3B and S3**), resulting in a connected network of interactions where only the Netrin  
182 axis remained unconnected in the extracellular space (**Figure 3A**). It should be noted that the  
183 DCC class of Netrin receptors were shown previously to interact with the Robo receptor  
184 intracellularly.<sup>25</sup> We also identified two novel ligands for Netrin receptors: PXN-1, a peroxidase  
185 associated with neuronal phenotypes,<sup>26</sup> interacting with UNC-5; and FMIL-1, an adhesion GPCR,  
186 interacting with UNC-40/DCC.

187 Given the central importance of axonal guidance pathways to neuronal wiring and their  
188 involvement in neurodevelopmental disorders, we chose to further validate these interactions with  
189 orthogonal methods. First, we performed ECIA experiments with protein domains to learn about  
190 the architectures of these new complexes. We showed that the IG domains of SAX-3/Robo bind  
191 PLX-1 IPT domains 3 to 6, and EFN-4 domain 2 (**Figures 3C and 3D**). To confirm these data, we  
192 produced SAX-3 IG1-4, EFN-4 D2 and PLX-1 IPT3-6 domain constructs using the baculoviral  
193 expression system in lepidopteran cells, and purified them to homogeneity. Purified SAX-3 IG1-4  
194 and EFN-4 D2 can form a stable complex observed via size-exclusion chromatography (SEC)  
195 (**Figure 3E**). We also validated the interaction of the Semaphorin MAB-20 with the Ephrin EFN-  
196 4, using purified MAB-20 ectodomain with the first domain of EFN-4 with both ECIA and SEC  
197 (**Figures 3F and 3G**). Our results implicate the first domain of Ephrin/EFN-4 in interactions with  
198 its classical receptors (EPHs) and Semaphorins, and the second domain in its interactions with  
199 Robos. Interestingly, we did not observe Semaphorin or Robo interactions with the other *C.*  
200 *elegans* Ephrins, which suggests specialization of EFN-4 to integrate multiple cell surface signals.

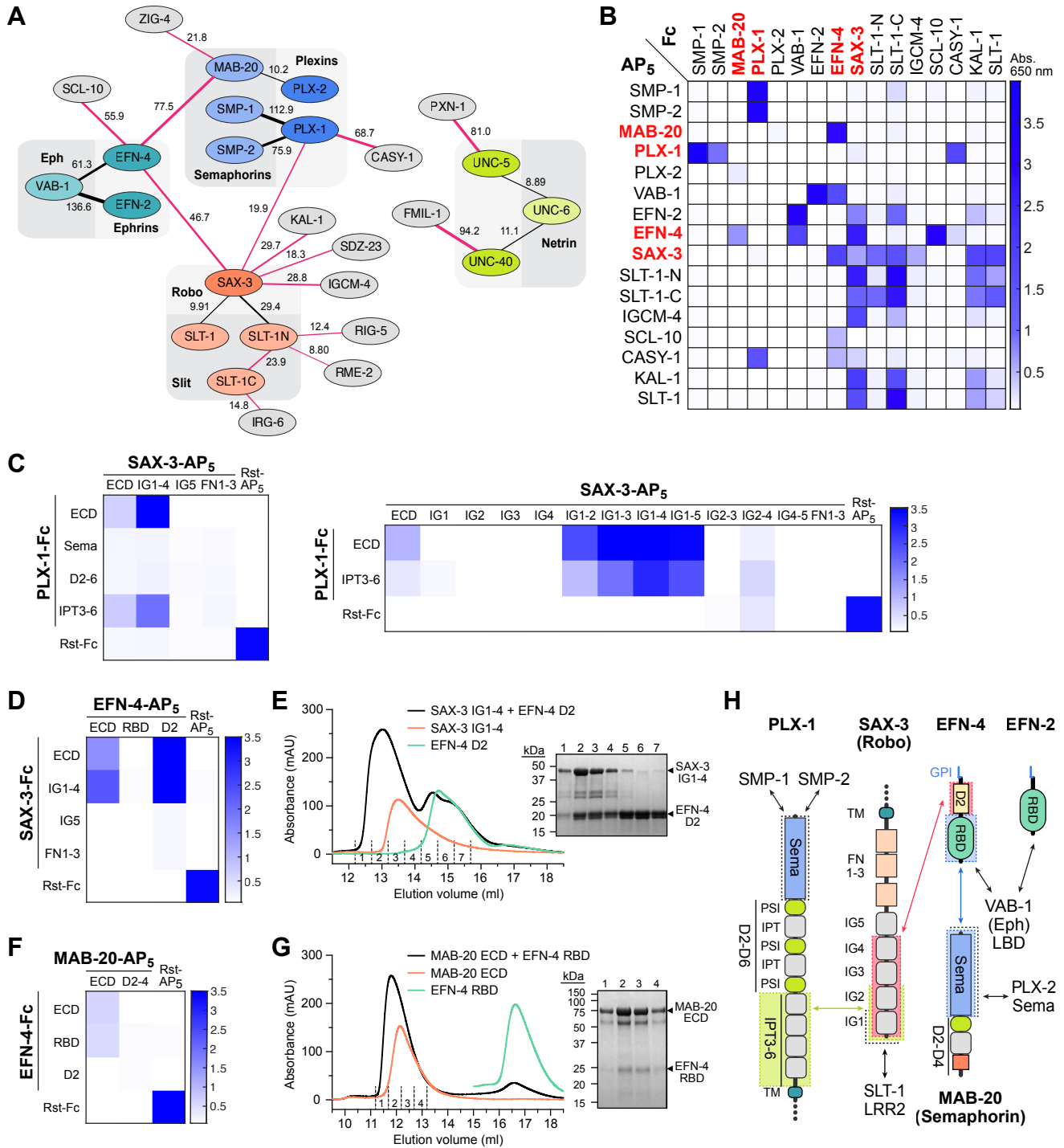


**Figure 3.** Axon guidance receptors and cues interact with each other outside the known cue-receptor axes.

**A.** Schematic of interactions from the high-throughput assay, where line thickness is scaled to symmetrized MaxEnt z-scores (Figure 2). Interactions that were not previously known are shown with red lines. The numbers next to the lines indicate z-scores. **B.** Interactions observed in the high-throughput assay are reproduced (see Figure S3 for more). As expected, interactions observed with a bait-prey (Fc-AP) pair are also observed in the reciprocal orientation, resulting in diagonally symmetrical assay results.

**C-G.** ECIA can be used to identify domains required for novel interactions: The first two IG domains of SAX-3 interact with the IPT domains 3 to 6 (C). SAX-3 IG domains also interact with the second domain of EFN-4, as observed by ECIA (D) and size-exclusion chromatography (SEC) (E). The interaction of MAB-20 with EFN-4 is mediated by the first domain (RBD) of EFN-4, as observed by ECIA (F) and SEC (G). SDS-polyacrylamide gels show the presence of both ectodomains in the complex fractions of SEC runs (E, G).

**H.** Summary of interactions between the domains of the axon guidance receptors and cues. Black arrows refer to interactions we observed but also previously characterized in other taxa.



201 *C. elegans* EFN-4 is also unique among Ephrins as we could not identify an EFN-4 D2-like  
202 sequence in other Ephrins outside nematodes.

### 203 **A family of insulin-receptor complexes revealed in nematodes**

204 Insulin and related peptides are conserved peptide hormones that regulate metabolism, cell  
205 proliferation, aging and longevity across animals through a conserved set of downstream  
206 signaling molecules, starting at the cell membrane through insulin receptors (IR) and the related  
207 Insulin-like growth factor receptors (IGFR).<sup>27–29</sup> In nematodes, the insulin family has expanded to  
208 a set of 40 insulin-like peptides (ILPs: INS-1 to -39 and DAF-28),<sup>30,31</sup> compared to only eight in *D.*  
209 *melanogaster* and ten in humans. Most nematode ILPs are expressed in neurons,<sup>32</sup> and they are  
210 proposed to act through the only insulin receptor, DAF-2, in *C. elegans*.<sup>27</sup> Depending on the  
211 context, ILPs have been observed to be agonists or antagonists of DAF-2,<sup>33</sup> which presents a  
212 mechanistic conundrum in the absence of co-ligands or co-receptors that may modulate DAF-2  
213 signaling in response to insulin-like peptides.

214 To advance our understanding of insulin signaling in *C. elegans*, we included four insulins (INS-  
215 1, INS-6, INS-18 and DAF-28) in our interaction screen. We observed that two insulins, DAF-28  
216 and INS-6, interact with ZIG-2 and ZIG-4, respectively (**Figure 2 and Table S3**). We also  
217 observed that ZIG-3 interacts with INS-6 and ZIG-5 interacts with INS-1. Multiple lines of evidence  
218 led us to classify ZIG-2 to -5 as a novel class of insulin-binding proteins distinct from other ZIGs:  
219 (1) Our sequence alignments of ZIG molecules, previously classified as neuronal surface or  
220 secreted proteins containing two-immunoglobulin domains, showed that ZIG-2 to -5 are closely  
221 related to each other and not to other ZIGs (**Figure 4A**); (2) ZIG-2 to -5 share sequence features  
222 uncommon to other IgSF proteins, especially at the linker connecting the two IG domains,  
223 including a disulfide bond (**Figure S4A**); and (3) ZIG-2 to -5 are all secreted, where most other  
224 ZIGs appear to have transmembrane helices or GPI membrane anchors (**Table S1**). Finally, ZIG-  
225 2 to -5 are co-expressed in the PVT neuron, along with ZIG-1 and -8, and have been implicated  
226 in the maintenance of axon position in the ventral nerve chord, suggesting a functional connection  
227 among these proteins.<sup>34,35</sup>

228 Next, we wanted to answer if other nematode insulins interact with ZIGs. To answer this question,



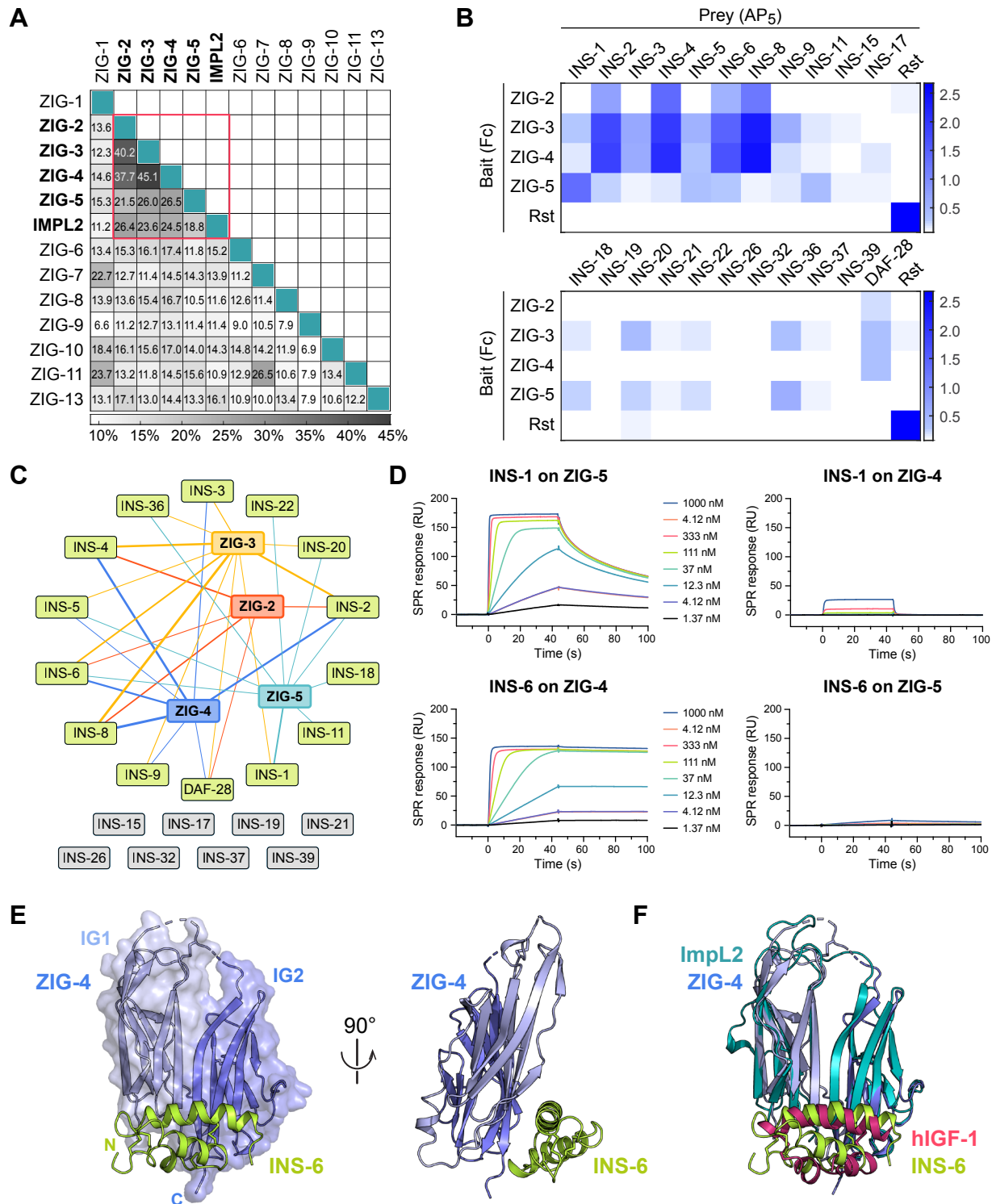


**Figure 4.** ZIG-2, -3, -4 and -5 make up a family of insulin-binding IgSF proteins.

**A.** Pairwise sequence identities show that ZIG-2 to -5 are more closely related to each other and to *Drosophila* Impl2 than the rest of the ZIG family.

**B.** ECIA for 22 insulin family members against ZIG-2 to -5. For expression levels of ZIGs and insulins, see Figures S4C, S4D.

**C.** ZIG-insulin interaction network inferred from the ECIA shown in B. The thickness of the connecting lines reflects the absorbance values in B for each ZIG-insulin interaction.

**D.** SPR sensorgrams for INS-1 and INS-6 binding to ZIG-5 and ZIG-4 immobilized on SPR chips. Kinetic fits with estimated on- and off-rates and equilibrium constants are shown in Figure S4E.

**E.** The structure of ZIG-4 (purple) bound to INS-6 (green) as observed in our tetragonal crystals.

**F.** The structure of the ZIG-4-INS-6 complex strongly resembles that of *Drosophila* Impl2 bound to human IGF-1 (PDB ID: 6FF3).

229 we created ECIA expression constructs for 18 other diverse insulins via RT-PCR, covering all  
230 three classes of *C. elegans* insulins.<sup>32</sup> When we repeated ECIA with these four ZIGs against the  
231 expanded set of 22 insulins, we observed binding between the four ZIGs and several other  
232 Insulins (**Figures 4B, 4C and S4B**). Since the ECIA signal depends on expression levels of bait  
233 and prey, which are different among the ZIGs and among the insulins (**Figures S4C and S4D**),  
234 we cannot compare affinities between various ZIG–Insulin interactions. However, we observed a  
235 trend where the  $\beta$ -class of insulins (INS-1 to -10 and DAF-28) gave higher signals of binding  
236 compared to other classes. Different binding specificities and affinities of insulins against the ZIG  
237 proteins may provide one means of differentiating their activities, even though all insulins likely  
238 act through the same receptor (DAF-2).

239 To validate these results, we performed SPR experiments for two pairs of insulins and ZIGs. ECIA  
240 results suggested that INS-6 binds most strongly to ZIG-4, while INS-1 binds most strongly to  
241 ZIG-5. SPR results confirmed these findings (**Figures 4D and S4E**), yielding dissociation  
242 constants ( $K_D$ ) for INS-1 binding to ZIG-5 and INS-6 binding to ZIG-4 were 3 nM and 56 pM, while  
243 the cross pairs had  $K_D > 1 \mu\text{M}$ . The very strong affinities observed suggest that insulins are  
244 unlikely to be free of ZIGs in contexts where ZIG-2 to -5 are expressed and secreted.

245 For more insights into the function of ZIG-insulin complexes, we crystallized the ZIG-4–INS-6  
246 complex and determined its crystal structure in three different crystal forms (**Figure 4E**). All three  
247 structures reveal the same complex (**Figure S4F**) and show that the two immunoglobulin domains  
248 of ZIG-4 create a continuous sheet made from the *ABE* strands of IG1 and the *ACFG* strands of  
249 IG2, to which INS-6 binds (**Figure 4E**). The ZIG-4-INS-6 structure is related to recently determined  
250 structures of a *Drosophila* IgSF protein ImpL2 bound to *Drosophila* DILP5 and to human IGF-1,<sup>36</sup>  
251 the atypical features of the two IG domains of ImpL2 are preserved in ZIG-4, and the overall root-  
252 mean-square displacement between the two structures is 1.4 Å over 158 (out of 202) C $\alpha$  atoms  
253 (**Figure 4F**). Indeed, ZIG-2 to -5 are more closely related to ImpL2 than to other *C. elegans* ZIGs  
254 (**Figure 4A**). These similarities imply that the ancestral ecdysozoan had a ZIG-2–5/ImpL2-like  
255 protein able to interact with insulin(s). We could not identify any ZIG-4 or ImpL2 orthologs in  
256 vertebrates; however, we found ZIG-2 to -5 and ImpL2-like sequences across protostome  
257 genomes. *Drosophila* ImpL2 has been proposed as a molecule aiding the bioavailability of insulins,

258 similar to vertebrate IGFbps, despite sharing no ancestry, structural or sequence similarities with  
259 IGFbps.<sup>36</sup> Therefore, it is possible that ZIG-2 to -5 may be functionally related to IGFbps in  
260 vertebrates, while not being related in sequence or structure.

261 As *Drosophila* and nematode insulins share the unexpected ability to act as both agonists and  
262 antagonists of insulin/IGF receptor,<sup>31</sup> we analyzed how ZIG-binding to insulins could control  
263 insulin activation of the insulin/IGF receptor. We first overlaid the ZIG-4-INS-6 structure on the  
264 crystal structure of human Insulin bound to a minimal insulin receptor (IR) fragment, including the  
265 L1 domain, the Cys-rich domain, the L2 domain and the C-terminal  $\alpha$ -helix ( $\alpha$ CT).<sup>37</sup> We saw that  
266 a ternary complex of INS-6, ZIG-4 and the insulin receptor was possible, where ZIG-4 was  
267 positioned to further interact with the IR, and not clash with it (**Figure S4G**). However, when the  
268 structure of the INS-6–ZIG-4 complex was aligned with any of the structural models of the dimeric  
269 IR bound with up to four insulins, presumably in partial or fully active states of the complex (e.g.,  
270 **Figure S4H**),<sup>38</sup> we observed that ZIG-4 severely clashes with one of the IR protomers forming the  
271 dimeric form of the IR complex, while aligning INS-6 with the site 1 insulin (**Figure S4I**). Similarly,  
272 the second insulin-binding site on IR overlaps with the ZIG-4-binding site, which would prevent  
273 the T-shaped IR<sub>2</sub>-insulin<sub>4</sub> from forming (**Figure S4J**). Therefore, when ZIGs are present, insulin  
274 receptor may be able to bind insulins, but will be sequestered in an inactive form, unable to make  
275 interactions with both protomers to form an active-state IR dimer. This presents an attractive and  
276 testable mechanism for how nematode and arthropod insulins may act as antagonists of DAF-  
277 2/insulin receptor.

## 278 **Cystine-knot proteins, putative neurotrophins, growth factors and their receptors in *C.*** 279 ***elegans***

280 As we curated *C. elegans* proteins that are on the cell surface or are secreted, we came across  
281 several proteins sharing common growth factor and cytokine-like folds. These include cystine-  
282 knot proteins, as well as FGF-like growth factors, and other molecules with growth factor-like  
283 sequences. We included several of these molecules in our ectodomain collection (annotated in  
284 **Table S1**) and identified binding partners for them.

285 First, we observed that two related cystine-knot family proteins, ZK856.6 and B0416.2, are the

286 strongest candidates for being ligands for TRK-1 (at  $z = 22.7$  and  $6.3$ , respectively), the  
287 designated *C. elegans* ortholog of the vertebrate high-affinity neurotrophin receptors, the Trk  
288 family of receptor tyrosine kinases (RTK) (**Figure 5A**). These two secreted proteins are, therefore,  
289 putative neurotrophins, a class of growth factors necessary for neuronal growth, survival and  
290 regeneration.<sup>39</sup> Vertebrate neurotrophins (NGF, BDNF, NT3 and NT4) are similarly Cys-knot  
291 proteins.<sup>40</sup> Searches for homologs of the two putative neurotrophins using BLAST returned no  
292 human, mouse or fly proteins, and only each other when searched for *C. elegans* paralogs. This  
293 demonstrates that interaction screening is more effective in identifying Cys-knot ligand-receptor  
294 pairs than using sequence similarity to known pairs. To confirm our findings, we expressed and  
295 purified the TRK-1 ectodomain and one of the putative neurotrophins ZK856.6, and performed  
296 SPR experiments, which validated the interaction (**Figure 5B**). Last, structural modeling using  
297 AlphaFold-multimer showed ZK856.6 and B0416.2 dimers interacting with the FN domains of  
298 TRK-1 in a manner reminiscent of vertebrate Neurotrophin-Trk Receptor complexes (**Figure S5**),  
299 supporting our claim that TRK-1 and its interactors may signal and function similarly to  
300 neurotrophin-receptor systems in vertebrates. Interestingly, one of the putative neurotrophins,  
301 ZK856.6, is a hub also interacting with C25E10.7, F15B9.8, LAG-2 (a Jagged/Delta homolog) and  
302 DEX-1.

303 Among the family of Cys-knot family of secreted proteins, we observed that B0222.11, C02B8.12  
304 and T16H12.9 interact with one receptor, HIR-1. This receptor was recently identified to direct  
305 hypoxia response and hypoxia-associated remodeling of the extracellular matrix.<sup>41</sup> HIR-1 is also a  
306 tyrosine kinase (RTK) with a cytoplasmic domain that resembles vertebrate RET and Fibroblast  
307 growth factor (FGF) receptors (FGFR). Based on this sequence similarity, the FGF homolog LET-  
308 756, which is a growth factor but not of the Cys-knot fold, was proposed as a potential HIR-1  
309 ligand.<sup>41</sup> Instead, we recommend that Cys-knot family proteins, including the three HIR-1 ligands,  
310 should be studied for hypoxia response in *C. elegans*. To validate our findings, we tested HIR-1  
311 ectodomain against B0222.22 and LET-756/FGF with SPR using purified proteins (**Figure 5C**).  
312 We observed a high-affinity complex of HIR-1 with B0222.22 ( $K_D = 0.50$  nM) (**Figure S5E**), while  
313 LET-756/FGF showed no binding to HIR-1.

314 We had included the two FGFs (EGL-17 and LET-756) and the FGFR ortholog (EGL-15) in our

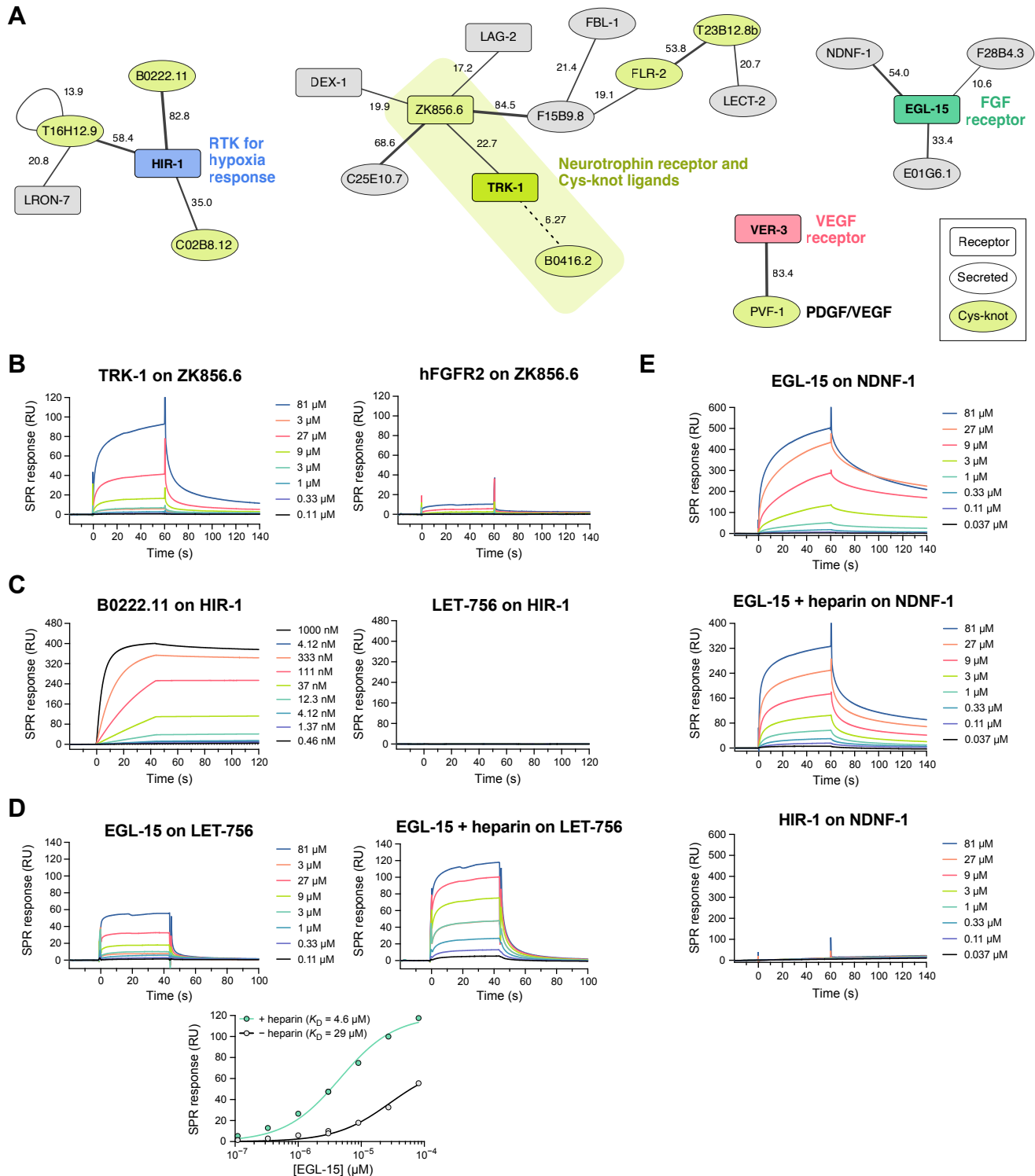


**Figure 5.** Networks of interactions with growth factor-like molecules and receptors.

**A.** Network of interactions between cytokine- and growth factor-like molecules and receptors as observed in our screen (Figure 2). Line thickness corresponds to the symmetrized z-scores for each interaction. The numbers next to the lines indicate the z-score values.

**B.** SPR sensorgrams for the interaction of TRK-1 with immobilized ZK856.6 and negative control (hFGFR2 against ZK856.6).

**C.** SPR sensorgrams for the interaction of B0222.11 with immobilized HIR-1 and negative control (LET-756 against HIR-1). Kinetic fits and parameters are shown in Figure S5E.

**D.** SPR sensorgrams and binding isotherms for the interaction of EGL-15 with immobilized LET-756 in the presence or absence of 50  $\mu\text{g}/\text{mL}$  (3.1  $\mu\text{M}$ ) heparin.

**E.** SPR sensorgrams for the interaction of EGL-15 with immobilized Fc-tagged NDNF-1 and negative control (HIR-1 against NDNF-1-Fc).

315 ectodomain collection. Surprisingly, we did not observe an interaction between these putative  
316 FGFs and the FGF receptor in our screen, likely as a result of complete lack of expression of the  
317 FGF ligands using our bait and prey plasmids in S2 cells (**Table S1**). To confirm this, we  
318 expressed and purified EGL-15/FGFR ectodomain and LET-756/FGF using lepidopteran cells  
319 and performed SPR experiments, which demonstrated the FGF-FGFR interaction in *C. elegans*  
320 (**Figure 5D**). This confirms that the lack of an FGF-FGFR hit in our screen is a false negative and  
321 was due to lack of protein expression. We observed stronger binding in the presence of heparin  
322 (**Figure 5D**), as previously observed for vertebrate FGFR-FGF interactions.<sup>42</sup>

323 In our screen, we observed NDNF-1, the nematode ortholog of the human neuron-derived  
324 neurotrophic factor, interacting with EGL-15/FGFR. NDNF and FGF are not homologous and do  
325 not share structural similarities, and an NDNF-FGFR interaction was not previously suspected or  
326 reported. However, NDNF overexpression is known to inhibit FGF signaling in cultured vertebrate  
327 cells, and FGFR-1 and NDNF are both implicated in congenital hypogonadotropic hypogonadism  
328 (CHH) and Kallmann syndrome (KS).<sup>43,44</sup> Our discovery of an NDNF-FGFR complex, may provide  
329 the missing mechanistic link that connects NDNF with FGFR signaling, especially in disease  
330 states.

331 To validate the interaction of NDNF-1 with EGL-15/FGFR, we set out to express NDNF, but failed  
332 to produce stable protein with common expression systems. Therefore, we used Protein A-  
333 coupled SPR chips to capture Fc-tagged NDNF-1, originally produced as bait for ECIA, and  
334 measured binding to EGL-15 as an SPR analyte. We observed strong binding in the absence and  
335 presence of heparin (**Figure 5E**), demonstrating the validity of the NDNF-1–EGL-15/FGFR  
336 interaction.

337 Finally, *C. elegans* has a single platelet-derived growth factor (PDGF) homolog, PVF-1. In our  
338 screen, we observed that PVF-1 binds VER-3, the predicted PDGF/VEGF receptor ortholog,  
339 suggesting that the PDGF/VEGF-mediated biology is conserved from nematodes to mammals.

### 340 ***C. elegans* Wirins: ZIG-8 and RIG-5 and their interactions**

341 An important result of our previous interactome study was the discovery of Dpr and DIP protein  
342 families (32 total members) in the fruit fly.<sup>4</sup> Dprs and DIPs interact with each other, and have been



343 strongly associated with synaptic specificity, axon guidance and fasciculation, cell fate  
344 determination and survival, and animal behavior.<sup>45</sup> We recently identified the nematode  
345 homologues of Dprs and DIPs, ZIG-8 and RIG-5, respectively, as part of a conserved family  
346 named Wirins,<sup>45</sup> and our interactome dataset reports a high-confidence ZIG-8–RIG-5 interaction  
347 as expected (**Table S3**). While homophilic and heterophilic interactions between Dprs and DIPs,  
348 and among their vertebrate orthologs (IgLONs) have been well established by others and us, it is  
349 unclear how Dprs and DIPs signal since they are GPI anchored proteins with no intracellular  
350 domains.<sup>46</sup> No extracellular cell surface receptors have been reported as binding partners for Dprs  
351 and DIPs to-date.

352 In our dataset, we observed several interactions with ZIG-8/Dpr and RIG-5/DIP (**Figure 6A**).  
353 These include ZIG-8 binding to C34C6.3, and RIG-5 interactions with B0507.1, PTP-3, NLR-1,  
354 T19D12.6 and HMR-1. Among the binding partners, NLR-1, T19D12.6 and HMR-1 belong to the  
355 LamG+EGF family of proteins, most prominently represented by the synaptic Neurexin proteins.  
356 NLR-1 is the *C. elegans* ortholog of Contactin-associated proteins (CNTNAP), known as NrX-IV  
357 in flies. Since CNTNAPs are known to take part in the formation of various types of cell junctions  
358 (such as *C. elegans* gap junctions, *Drosophila* septate junctions and vertebrate axo-glial  
359 junctions),<sup>47–50</sup> and have known neuronal and synaptic developmental functions,<sup>51,52</sup> they are  
360 plausible candidates for mediating Dpr/DIP signaling. The other strong candidate interaction for  
361 mediating Dpr/DIP signaling is the RIG-5–PTP-3 interaction: PTP-3 is a receptor protein tyrosine  
362 phosphatase (RPTP) and the worm ortholog for LAR. LAR has been implicated in *Drosophila* to  
363 control synaptic development and signaling in the photoreceptor cells and neuromuscular  
364 junctions,<sup>53,54</sup> where Dpr-DIP was previously shown to control synaptic signaling.<sup>55</sup> HMR-1 has  
365 been shown to be required for axon fasciculation and dendrite extension in *C. elegans*,<sup>56–58</sup> and  
366 its fly ortholog, CadN, functions in synaptic targeting in the developing optic lobe;<sup>59,60</sup> Dprs and  
367 DIPs are similarly known to control synaptic targeting of photoreceptor neurons.<sup>55</sup> These strong  
368 functional links support the validity of these interactions. To further confirm these interactions, we  
369 performed SPR with purified RIG-5 ectodomain against PTP-3, NLR-1 and HMR-1 ectodomains,  
370 and validated the interaction hits (**Figures 6B-E**). These interactions proved to be lower affinity,  
371 as would be expected for co-receptors residing on the same cell, which may also require the



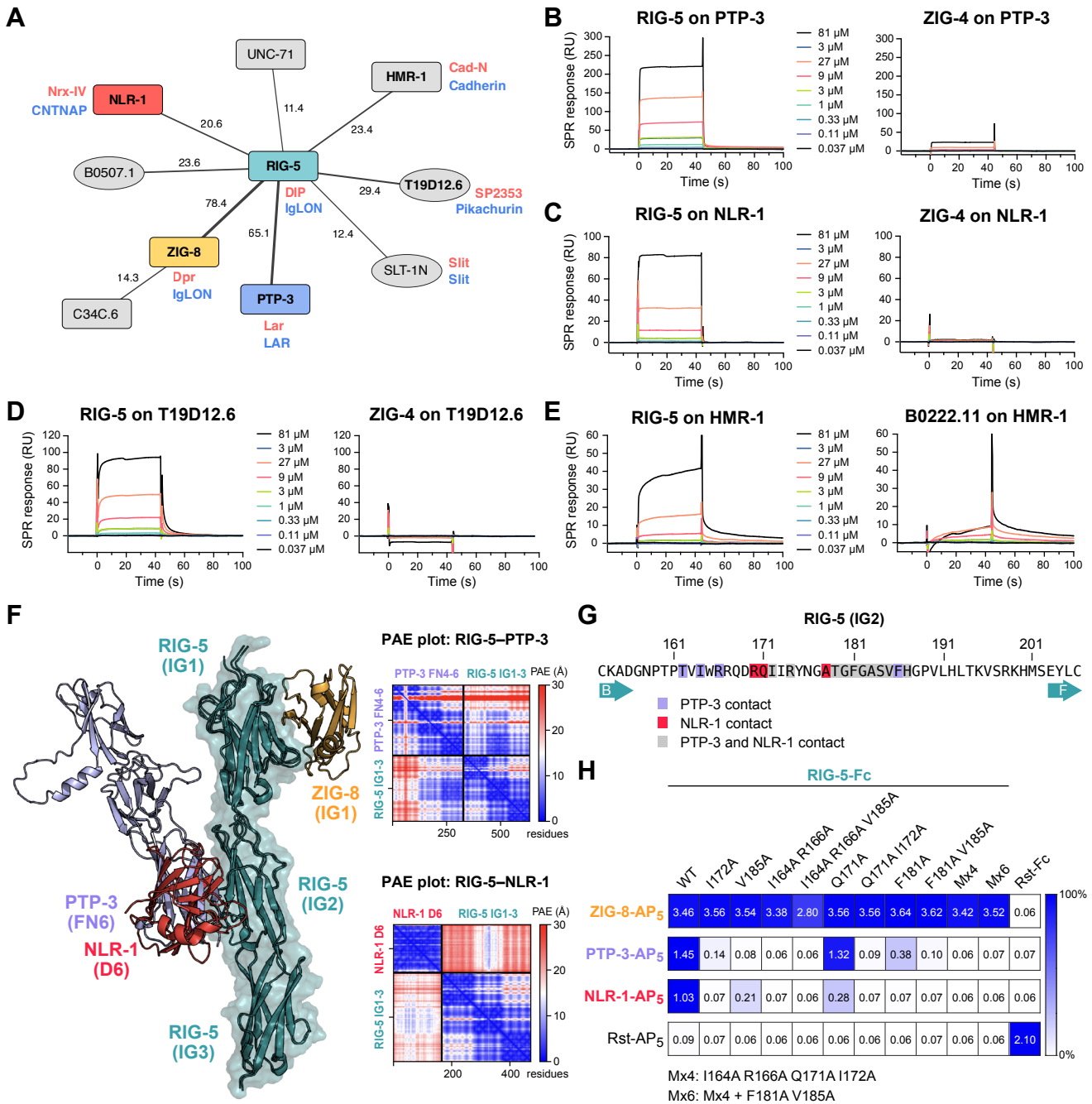


**Figure 6.** RIG-5 interacts with molecules with neuronal and synaptic functions.

**A.** Interactions of ZIG-8/Dpr and RIG-5/DIP according to our screen. Red and blue names represent orthologs in *D. melanogaster* and mammals, respectively. Line thickness scales with the symmetrized z-scores for each interaction. The numbers next to the lines indicate the z-score values.

**B-E.** SPR sensorgrams for interactions of RIG-5 with immobilized PTP-3 (B), NLR-1 (C), T19D12.6 (D), and HMR-1 (E).

**F.** Overlay of the ZIG-8–RIG-5 structure (PDB ID: 6ON9) (Cheng *et al.*, 2019) and AlphaFold-multimer models for RIG-5 IG1-3+NLR-1 D6 and RIG-5 IG1-3+PTP-3 FN4-6. ZIG-8/Dpr binding to RIG-5/DIP does not overlap with PTP-3 and NLR-1, which share a binding site on the RIG-5 IG2 domain. See Figure S6 for details of the AlphaFold-predicted interfaces. Predicted aligned error (PAE) plots for AlphaFold predictions are shown for both RIG-5 (ECD)-PTP-3 (FN4-6) and RIG-5 (ECD)-NLR-1 (D6) complexes.

**G.** RIG-5 IG2 residues identified to interact with PTP-3 and NLR-1 in AlphaFold models.

**H.** ECIA for RIG-5 ECD mutants against ZIG-8, PTP-3 and NLR-1 ECDs. Mutations in RIG-5 IG2 that break PTP-3 and NLR-1 binding do not affect ZIG-8 binding, which is known to happen through the IG1 domain. The raw readout for the assay (absorbance at  $\lambda = 650$  nm) is noted in each square. The homodimeric Rst interaction is a positive control.

372 formation of high-density ZIG-8/Dpr–RIG-5/DIP clusters.

373 To gain further insights into some of these interactions, we used the Colabfold implementation of  
374 AlphaFold2-Multimer.<sup>61,62</sup> We predicted models for both the RIG-5–PTP-3 and RIG-5–NLR-1  
375 complexes with reasonable ipTM (interface predicted template modeling) values (0.72 and 0.49,  
376 respectively) and predicted aligned error (PAE) values (**Figure 6F**), where the second IG domain  
377 of RIG-5/DIP interacts with these signaling receptors using highly overlapping interfaces (**Figures**  
378 **6F, 6G and S6**). We designed point mutations of RIG-5 that are likely to break these interactions,  
379 and tested them for binding via ECIA (**Figure 6H**): We observed that the mutations broke the  
380 PTP-3 and NLR-1 complexes of RIG-5 as predicted, but none affected ZIG-8/Dpr binding, which  
381 depends on an epitope on the first IG domain.<sup>45,55</sup> These results support our RIG-5 interaction  
382 discovery, as well as the AlphaFold prediction of the binding interfaces. We suggest that the study  
383 of Dprs and DIPs in the fly model should include the orthologs Lar, NrX-4 and CadN, to reveal  
384 Dpr-DIP signaling at the synapse.

### 385 **Limitations of the ECIA screen and further insights**

386 While we observed many interactions that were previously known, there were some expected  
387 complexes that we did not observe. As mentioned above, the FGF-FGFR complexes were missed  
388 likely as a result of lack of FGF expression in our expression system. 23% of our constructs did  
389 not yield detectable expression, as judged by western blotting (**Table S1**), which is likely the  
390 largest source of false negatives. However, there are other unexpected negatives that cannot be  
391 explained by lack of expression based on known binding data with vertebrate homologs. One  
392 such case is the lack of binding between LAT-1 and TEN-1, the nematode homologs of  
393 Latrophilins and Teneurins, which form a synapse-instructive complex in mammals. A previous  
394 study suggested that this interaction may not exist in invertebrates on the basis of genetic data,  
395 and therefore the nematode and mammalian Latrophilins and Teneurins may act through different  
396 ligands.<sup>63</sup> We report the Toll-like receptor TOL-1 and the LRR protein LRON-11 as interaction  
397 partners for LAT-1 and TEN-1 in *C. elegans*, respectively, and show in an accompanying paper  
398 that the LAT-1–TOL-1 complex is needed during early embryo development.<sup>64</sup> Another  
399 unexpected observation from the high-throughput assay was the lack of an interaction hit between  
400 Neurexin (NRX-1) and Neuroligin (NLG-1). Neurexins and Neuroligins are major regulators of

401 synapse formation and function, and interact strongly with each other.<sup>65</sup> However, biochemical  
402 proof of a direct interaction between *C. elegans* NRX-1 and NLG-1 is limited.<sup>66</sup> To scrutinize our  
403 unexpected negative result, we performed surface plasmon resonance experiments with the  
404 ectodomain of NLG-1 against the LNS6 domain of NRX-1, previously established as the domain  
405 responsible for Neuroligin interactions.<sup>67</sup> Unlike studies demonstrating nM affinity with comparable  
406 constructs of mammalian homologs,<sup>68,69</sup> we observed binding between nematode NRX-1 and  
407 NLG-1 with a ~48  $\mu$ M dissociation constant, about three orders of magnitude weaker than the  
408 mammalian orthologs (**Figures S7A and S7B**). Similarly, size-exclusion chromatography  
409 experiments showed no stable complex formation, unlike previous observations for mammalian  
410 Neurexin-Neuroligin complexes, but in agreement with a very weak complex (**Figure S7C**).<sup>70</sup>  
411 Therefore, it is possible that while nematode Neurexins and Neuroligins may have preserved their  
412 neuronal functions, they may mediate it through interactions via other proteins, such as with  
413 MADD-4,<sup>71</sup> via novel interaction partners we identified in our assay, such as TMEM132 for NRX-  
414 1, or heavily depend on other factors, such as heparan sulfate modifications of Neurexin as  
415 recently discovered<sup>72</sup> for strong complex formation.

#### 416 **AlphaFold-Multimer predictions for interactions observed by ECIA**

417 Since we observed that AlphaFold models have proven useful in revealing novel interactions from  
418 our dataset, we took a systematic approach to study if AlphaFold results may indicate complex  
419 formation. We calculated AlphaFold-multimer complexes for 72 high-confidence interactions we  
420 observed for complexes with <2500 amino acids, as well as 46 complexes created by randomly  
421 pairing proteins from the same set of proteins. We used the ipTM values reported by AlphaFold  
422 as a measure of its confidence for the complex model. Our observed complexes had an average  
423 ipTM value of  $0.495 \pm 0.241$ , while random protein pairs gave an average ipTM value of  $0.273 \pm$   
424  $0.139$  (**Figure 7A and Table S3**). The remarkable differences in the distribution of ipTM values  
425 for observed complexes vs. randomly paired proteins attest to the usefulness of AlphaFold as a  
426 predictor of protein complex formation, while also supporting our discovery results.

427 To analyze AlphaFold predictions further, we investigated whether observing higher ipTM values  
428 correlate with any property of our complexes. We observed no correlation between sequence  
429 length and ipTM (**Figure 7B**). However, ipTM values were significantly higher for complexes

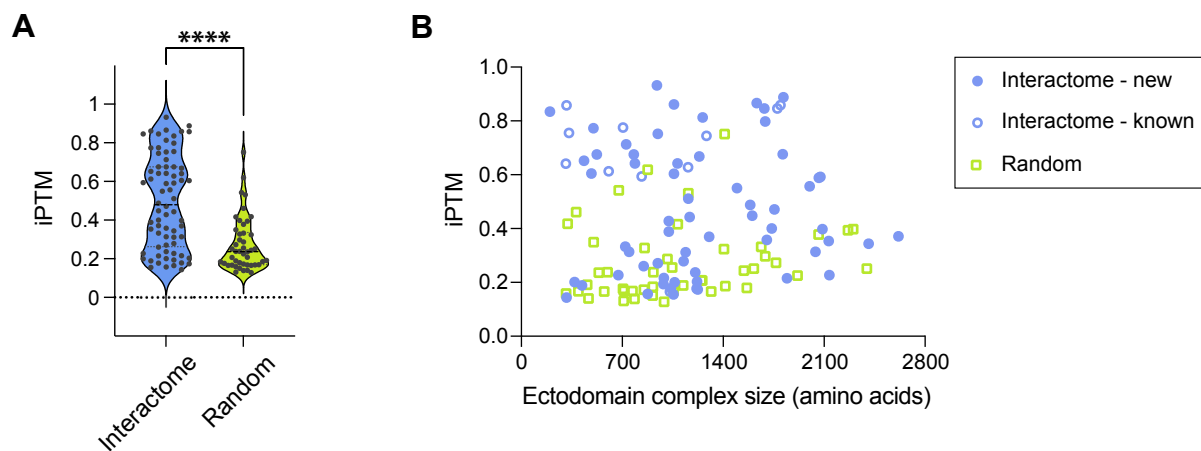


**Figure 7.** AlphaFold predictions of extracellular protein complexes and chemical synapses corresponding to PPIs.  
**A.** ipTM (interface predicted Template Modelling) score values of AlphaFold-predicted complexes from our interactome (blue) and random pairings of proteins (green).  
**B.** Size of the protein complex does not correlate with ipTM values. ECIA hits with previously determined homologous

430 which had homologous (mostly mammalian) complex structures in the Protein Data Bank ( $0.676$   
431  $\pm 0.190$ ). This is not surprising, as these structures were likely in the training set for AlphaFold-  
432 multimer. However, even after removing protein pairs with homologous complex structures in the  
433 PDB, the complexes we detected had significantly higher ipTM values on average ( $0.459 \pm 0.236$ )  
434 than randomly paired complexes, demonstrating that AlphaFold can be a useful tool in identifying  
435 novel protein complexes, and for studying the structures of these complexes. Computational  
436 pipelines using this idea have been established recently.<sup>73</sup>

### 437 **Chemical synapses corresponding to the observed interactions.**

438 Protein-protein interactions (PPIs) play a crucial role in forming chemical synapses between  
439 neurons.<sup>74</sup> Therefore, we investigated the chemical synapse connectome<sup>75</sup> associated with PPIs.  
440 Specifically, a PPI is considered as evidence that supports a chemical synapse if the  
441 corresponding genes are expressed in the neurons forming a chemical synapse. We used the  
442 gene expression data from CeNGEN.<sup>76</sup> Among the 134 PPIs that has available gene expression  
443 data related to chemical synapses, there are only 4 PPIs that do not serve as evidence of any  
444 known chemical synapses, namely ZC374.2–T02C5.1A, INS-6–ZIG-2, SGCA-1–IRLD-51, and  
445 LRON-7–T02C5.1A. The remaining 130 PPIs can potentially explain the entire known chemical  
446 synapse connectome. While 99.9% of chemical synapses have more than 5 evidences, there are  
447 a few examples of more specific chemical synapses. For example, HMR-1–HMR-1, IGCM-3–  
448 IGCM-3, and MAB-20–PLX-2 support the chemical synapses between the AVKL and AVKR  
449 neurons. Additionally, we have included the 185 experimental PPIs with the number of supporting  
450 synapses in **Table S7**. To establish a robust statistical framework for evaluating the significance  
451 of these interactions associated with the formation of chemical synapses, we implemented a  
452 randomized neuron connectome as a control. Our analysis revealed two distinct categories of  
453 noteworthy PPIs: (1) PPIs with the highest number of supporting synapses: TMEM-132–NRX-1,  
454 CASY-1–T19D12.6, PTP-3–NLR-1, CASY-1–PLX-1, SAX-3–PLX-1. These interactions are of  
455 particular interest due to their prevalence within the synaptic connectome, potentially indicating  
456 their functional importance in neuronal communication; (2) PPIs demonstrating the highest  
457 statistical significance when compared to the randomized control: SLT-1N–SLT-1C, LECT-2–  
458 MIG-13, UNC-5–PXN-1, ZIG-4–DAF-28, F15B9.8–ZK856.6. The statistical significance of these

459 PPIs suggests that their occurrence is non-random and may represent biologically relevant  
460 interactions worthy of further investigation. These results highlight significant putative  
461 contributions of experimental PPIs in unraveling the intricate complexities of chemical synapses.

462

## 463 **DISCUSSION**

464 Protein-protein interactions in the extracellular space control the development and functioning of  
465 all aspects of multicellular physiology. With this study, we report the results of an extracellular  
466 interaction screen of 379 *C. elegans* cell surface receptors and secreted proteins, the largest for  
467 a non-human species to-date, that covers a diverse range of the protein fold space. The  
468 interactions we report are mostly novel, even when counting those identified for orthologs in other  
469 taxa as previously known (86% previously unknown).

### 470 **Novel interactions among guidance cues and receptors for neuronal development and** 471 **animal morphogenesis**

472 In our ectodomain collection, we have included known axon guidance cues and receptors, and to  
473 our surprise, observed many novel interactions that link separate cue-receptor axes. This brings  
474 up the possibility that these interactions might build “supra-signaling complexes” able to  
475 incorporate cues and signaling receptors from multiple pathways. Based on our map of domain-  
476 domain interactions (**Figure 3H**), the Robo-Ephrin-Semaphorin (SAX-3–EFN-4–MAB-20), Robo-  
477 Ephrin-Eph (SAX-3–EFN-4–VAB-1) or Robo-Plexin-Semaphorin (SAX-3–PLX-1–SMP-1/2)  
478 supercomplexes may be possible, as the domains needed to form these complexes do not  
479 overlap. How these supra-molecular complexes would signal needs to be studied *in vivo*,  
480 especially in the light of expression patterns of these various proteins. It is also possible that some  
481 of the new interactions we identified act to silence the canonical pathways by blocking the  
482 formation of the known complexes: this may be the case for SAX-3/Robo, as all its binding  
483 partners interact with its IG domains. These interactions can be studied readily, thanks to the  
484 extensive collection of mutant strains, published genetic interactions, and expression data already  
485 available in *C. elegans*.



486 The interactions we identified between the separate axon guidance axes also highlight the  
487 multiple roles these receptors and ligands play. For example, morphogenesis of the intestine in  
488 *C. elegans* is known to be mediated by movements of cells governed by the actions of MAB-  
489 20/Semaphorin, SAX-3/Robo and EFN-4/Ephrin, which we have now identified to interact with  
490 each other.<sup>77</sup> Similarly, *efn-4* and *mab-20* mutant animals have highly similar phenotypes in  
491 axonal growth and guidance in the same cells,<sup>78,79</sup> as well as in epidermal enclosure of embryos,<sup>80</sup>  
492 and male tail morphogenesis.<sup>81,82</sup> Genetic interactions and shared phenotypes identified for these  
493 genes are likely due to the direct physical interactions we report here.

#### 494 **Growth factors and their receptors in *C. elegans***

495 We have identified cystine-knot binding partners for the *C. elegans* Trk-like receptor, TRK-1.  
496 Previous efforts to identify nematode neurotrophins and their receptors by sequence have not  
497 been successful.<sup>83</sup> Despite lack of apparent sequence similarity for both the vertebrate  
498 neurotrophins and the Trk receptor ectodomain, AlphaFold prediction of our newly identified  
499 complexes at 2:2 stoichiometry, show strong resemblances to the known structures of mammalian  
500 Trk receptors, neurotrophins and their complexes (**Figure S4**).<sup>84–86</sup>

501 We report additional interactions for growth factor-like molecules, one of which is the worm  
502 ortholog of the Neuron-derived neurotrophic factor, NDNF-1, interacting with EGL-15/FGFR. We  
503 suggest that this interaction may be the underlying reason for why NDNF and FGFR mutations  
504 are both found in human patients with congenital hypogonadotropic hypogonadism and Kallmann  
505 syndrome. The fruit fly NDNF, Nord, also binds with and regulates degradation of Dally, a  
506 glypican-type heparan sulfate proteoglycan.<sup>87,88</sup> Since FGF-FGFR interactions are strengthened  
507 by heparan sulfate (**Figure 5D**),<sup>56,57</sup> and that heparin does not break the NDNF-1-EGL-15/FGFR  
508 interaction (**Figure 5E**), it is reasonable to speculate that NDNF may interact with Dally/Glypican  
509 as well as FGF receptors, and prevent FGF from turning on FGFR signaling.

#### 510 **Interactomes for model organisms**

511 One important takeaway message we learned is that proper study of biological processes in a  
512 model organism requires dedicated effort in revealing the relevant biochemistry for that model  
513 organism. As one example, insulin signaling in *C. elegans* has been heavily studied and proven



514 insightful for understanding aging, neuronal and embryonic development. However, as we show  
515 here, more may need to be done to reveal the biochemical components of the system (such as  
516 ZIG-2 to -5) and their effects on signaling, which may or may not be shared with other model  
517 organisms.

518 Conversely, our interactome dataset will likely prove useful across many model organisms. For  
519 example, we revealed several new binding partners for the two *C. elegans* homologs of  
520 *Drosophila* Dprs and DIPs, which are a 32-member receptor family known for their roles in  
521 neuronal wiring in the fruit fly. Our findings will facilitate study of neuronal wiring in both model  
522 systems, given the novel signaling co-receptors we propose for this receptor family. In addition,  
523 the interactome dataset can be used in conjunction with expression data to identify candidate  
524 proteins and complexes with roles in any cell surface process in specific cell types, such as  
525 synapse formation. For example, expression of ZIG-8/Dpr and RIG-5/DIP are enriched in pairs of  
526 cells known to form synapses (**Table S7**).

## 527 **Towards a complete extracellular interactome**

528 Here, we report significant improvements to our extracellular interactome methodology, including  
529 a statistically rigorous method for data analysis, applicable to related interactome strategies and  
530 high-throughput ELISA-like assays. We also implemented enhancements to improve throughput;  
531 Additional gains in throughput can also be achieved by pooling of bait or prey, as recently done  
532 in Wojtowicz *et al.*<sup>8</sup> The largest obstacle for us has been the time and cost of creating the plasmid  
533 collection, while the entire assay could then be completed by two full-time researchers in only two  
534 months. As gene synthesis costs decrease significantly, complete interactomes of all receptors  
535 and secreted proteins will become cheaper to execute for several model organisms of interest, to  
536 support a more complete mechanistic understanding of development, health and disease.

## 537 **ACKNOWLEDGMENTS**

538 We would like to thank Kang Shen for guidance and sharing reagents, and Jingxian Li, Demet  
539 Araç, and Joseph S. Pak for technical and critical discussions, and Mateusz Krzyscik and Dengke  
540 Ma for sharing reagents. We acknowledge Hyun Lee and the University of Illinois at Chicago  
541 Biophysics Core Facility, and Elena Solomaha and the UChicago Biophysics Core Facility for

542 SPR access and help. E.Ö. and I.A.K. acknowledge both support from the National Institute for  
543 Theory and Mathematics in Biology through the National Science Foundation (grant number  
544 DMS-2235451) and the Simons Foundation (grant number MP-TMPS-00005320). This study  
545 used resources of the Advanced Photon Source (APS), a U.S. Department of Energy (DOE)  
546 Office of Science User Facility operated for the DOE Office of Science by Argonne National  
547 Laboratory under Contract No. DE-AC02-06CH11357. Crystallographic data was collected at  
548 Northeastern Collaborative Access Team beamlines, which are funded by the National Institute  
549 of General Medical Sciences from the NIH (P30 GM124165). The Eiger 16M detector on the 24-  
550 ID-E beam line is funded by a NIH-ORIP HEI grant (S10OD021527).

#### 551 **DECLARATION OF INTERESTS**

552 The authors declare no competing interests.

553

554 **REFERENCES**

- 555 1. Nichols, S.A., Dirks, W., Pearse, J.S., and King, N. (2006). Early evolution of animal cell  
556 signaling and adhesion genes. *Proc Natl Acad Sci U S A* *103*, 12451–12456.  
557 <https://doi.org/10.1073/pnas.0604065103>.
- 558 2. Santos, R., Ursu, O., Gaulton, A., Bento, A.P., Donadi, R.S., Bologa, C.G., Karlsson, A., Al-  
559 Lazikani, B., Hersey, A., Oprea, T.I., et al. (2017). A comprehensive map of molecular drug  
560 targets. *Nat Rev Drug Discov* *16*, 19–34. <https://doi.org/10.1038/nrd.2016.230>.
- 561 3. Bushell, K.M., Söllner, C., Schuster-Boeckler, B., Bateman, A., and Wright, G.J. (2008).  
562 Large-scale screening for novel low-affinity extracellular protein interactions. *Genome Res*  
563 *18*, 622–630. <https://doi.org/10.1101/gr.7187808>.
- 564 4. Özkan, E., Carrillo, R.A., Eastman, C.L., Weiszmann, R., Waghay, D., Johnson, K.G., Zinn,  
565 K., Celniker, S.E., and Garcia, K.C. (2013). An Extracellular Interactome of Immunoglobulin  
566 and LRR Proteins Reveals Receptor-Ligand Networks. *Cell* *154*, 228–239.  
567 <https://doi.org/10.1016/j.cell.2013.06.006>.
- 568 5. Wojtowicz, W.M., Wu, W., Andre, I., Qian, B., Baker, D., and Zipursky, S.L. (2007). A vast  
569 repertoire of Dscam binding specificities arises from modular interactions of variable Ig  
570 domains. *Cell* *130*, 1134–1145. <https://doi.org/10.1016/j.cell.2007.08.026>.
- 571 6. Visser, J.J., Cheng, Y., Perry, S.C., Chastain, A.B., Parsa, B., Masri, S.S., Ray, T.A., Kay,  
572 J.N., and Wojtowicz, W.M. (2015). An extracellular biochemical screen reveals that FLRTs  
573 and Unc5s mediate neuronal subtype recognition in the retina. *eLife* *4*, e08149.  
574 <https://doi.org/10.7554/eLife.08149>.
- 575 7. Smakowska-Luzan, E., Mott, G.A., Parys, K., Stegmann, M., Howton, T.C., Layeghifard, M.,  
576 Neuhold, J., Lehner, A., Kong, J., Grünwald, K., et al. (2018). An extracellular network of  
577 Arabidopsis leucine-rich repeat receptor kinases. *Nature* *553*, 342–346.  
578 <https://doi.org/10.1038/nature25184>.
- 579 8. Wojtowicz, W.M., Vielmetter, J., Fernandes, R.A., Siepe, D.H., Eastman, C.L., Chisholm,  
580 G.B., Cox, S., Klock, H., Anderson, P.W., Rue, S.M., et al. (2020). A Human IgSF Cell-  
581 Surface Interactome Reveals a Complex Network of Protein-Protein Interactions. *Cell* *182*,  
582 1027-1043.e17. <https://doi.org/10.1016/j.cell.2020.07.025>.
- 583 9. Verschueren, E., Husain, B., Yuen, K., Sun, Y., Paduchuri, S., Senbabaoglu, Y., Lehoux, I.,  
584 Arena, T.A., Wilson, B., Lianoglou, S., et al. (2020). The Immunoglobulin Superfamily  
585 Receptome Defines Cancer-Relevant Networks Associated with Clinical Outcome. *Cell* *182*,  
586 329-344.e19. <https://doi.org/10.1016/j.cell.2020.06.007>.
- 587 10. Li, H., Watson, A., Olechwier, A., Anaya, M., Sorooshyari, S.K., Harnett, D.P., Lee, H.-K.P.,  
588 Vielmetter, J., Fares, M.A., Garcia, K.C., et al. (2017). Deconstruction of the Beaten Path-  
589 Sidestep interaction network provides insights into neuromuscular system development.  
590 *eLife* *6*, e28111. <https://doi.org/10.7554/eLife.28111>.
- 591 11. Söllner, C., and Wright, G.J. (2009). A cell surface interaction network of neural leucine-rich  
592 repeat receptors. *Genome Biol* *10*, R99. <https://doi.org/10.1186/gb-2009-10-9-r99>.
- 593 12. Corsi, A.K., Wightman, B., and Chalfie, M. (2015). A Transparent Window into Biology: A  
594 Primer on *Caenorhabditis elegans*. *Genetics* *200*, 387–407.  
595 <https://doi.org/10.1534/genetics.115.176099>.

- 596 13. Vogel, C., and Chothia, C. (2006). Protein family expansions and biological complexity.  
597 PLoS Comput Biol 2, e48. <https://doi.org/10.1371/journal.pcbi.0020048>.
- 598 14. Wright, G.J. (2009). Signal initiation in biological systems: the properties and detection of  
599 transient extracellular protein interactions. Mol Biosyst 5, 1405–1412.  
600 <https://doi.org/10.1039/B903580J>.
- 601 15. Vogel, C., Teichmann, S.A., and Chothia, C. (2003). The immunoglobulin superfamily in  
602 Drosophila melanogaster and Caenorhabditis elegans and the evolution of complexity.  
603 Development 130, 6317–6328. <https://doi.org/10.1242/dev.00848>.
- 604 16. Hobert, O., Hutter, H., and Hynes, R.O. (2004). The immunoglobulin superfamily in  
605 Caenorhabditis elegans and Drosophila melanogaster. Development 131, 2237–2238;  
606 author reply 2238–2240. <https://doi.org/10.1242/dev.01183>.
- 607 17. Huynh, C.Q., and Zieler, H. (1999). Construction of modular and versatile plasmid vectors  
608 for the high-level expression of single or multiple genes in insects and insect cell lines. J Mol  
609 Biol 288, 13–20. <https://doi.org/10.1006/jmbi.1999.2674>.
- 610 18. Lee, D.F., Chen, C.C., Hsu, T.A., and Juang, J.L. (2000). A baculovirus superinfection  
611 system: efficient vehicle for gene transfer into Drosophila S2 cells. J Virol 74, 11873–11880.  
612 <https://doi.org/10.1128/jvi.74.24.11873-11880.2000>.
- 613 19. Kovács, I.A., Barabási, D.L., and Barabási, A.-L. (2020). Uncovering the genetic blueprint of  
614 the C. elegans nervous system. Proc Natl Acad Sci U S A 117, 33570–33577.  
615 <https://doi.org/10.1073/pnas.2009093117>.
- 616 20. Spirin, V., and Mirny, L.A. (2003). Protein complexes and functional modules in molecular  
617 networks. Proc Natl Acad Sci U S A 100, 12123–12128.  
618 <https://doi.org/10.1073/pnas.2032324100>.
- 619 21. Lambiotte, R., Delvenne, J.-C., and Barahona, M. (2014). Random Walks, Markov  
620 Processes and the Multiscale Modular Organization of Complex Networks. IEEE Trans  
621 Netw Sci Eng 1, 76–90. <https://doi.org/10.1109/TNSE.2015.2391998>.
- 622 22. Alther, T.A., Domanitskaya, E., and Stoeckli, E.T. (2016). Calsyntenin 1-mediated trafficking  
623 of axon guidance receptors regulates the switch in axonal responsiveness at a choice point.  
624 Development 143, 994–1004. <https://doi.org/10.1242/dev.127449>.
- 625 23. Ruiz de Almodovar, C., Fabre, P.J., Knevels, E., Coulon, C., Segura, I., Haddick, P.C.G.,  
626 Aerts, L., Delattin, N., Strasser, G., Oh, W.-J., et al. (2011). VEGF mediates commissural  
627 axon chemoattraction through its receptor Flk1. Neuron 70, 966–978.  
628 <https://doi.org/10.1016/j.neuron.2011.04.014>.
- 629 24. Bashaw, G.J., and Klein, R. (2010). Signaling from axon guidance receptors. Cold Spring  
630 Harb Perspect Biol 2, a001941. <https://doi.org/10.1101/cshperspect.a001941>.
- 631 25. Yu, T.W., Hao, J.C., Lim, W., Tessier-Lavigne, M., and Bargmann, C.I. (2002). Shared  
632 receptors in axon guidance: SAX-3/Robo signals via UNC-34/Enabled and a Netrin-  
633 independent UNC-40/DCC function. Nat Neurosci 5, 1147–1154.  
634 <https://doi.org/10.1038/nn956>.
- 635 26. Lee, J., Bandyopadhyay, J., Lee, J.I., Cho, I., Park, D., and Cho, J.H. (2015). A role for  
636 peroxidase PXN-1 in aspects of C. elegans development. Mol Cells 38, 51–57.

- 637 <https://doi.org/10.14348/molcells.2015.2202>.
- 638 27. Kimura, K.D., Tissenbaum, H.A., Liu, Y., and Ruvkun, G. (1997). *daf-2*, an insulin receptor-  
639 like gene that regulates longevity and diapause in *Caenorhabditis elegans*. *Science* 277,  
640 942–946. <https://doi.org/10.1126/science.277.5328.942>.
- 641 28. Brogiolo, W., Stocker, H., Ikeya, T., Rintelen, F., Fernandez, R., and Hafen, E. (2001). An  
642 evolutionarily conserved function of the *Drosophila* insulin receptor and insulin-like peptides  
643 in growth control. *Curr Biol* 11, 213–221. [https://doi.org/10.1016/s0960-9822\(01\)00068-9](https://doi.org/10.1016/s0960-9822(01)00068-9).
- 644 29. Hua, Q.-X., Nakagawa, S.H., Wilken, J., Ramos, R.R., Jia, W., Bass, J., and Weiss, M.A.  
645 (2003). A divergent INS protein in *Caenorhabditis elegans* structurally resembles human  
646 insulin and activates the human insulin receptor. *Genes Dev* 17, 826–831.  
647 <https://doi.org/10.1101/gad.1058003>.
- 648 30. Duret, L., Guex, N., Peitsch, M.C., and Bairoch, A. (1998). New insulin-like proteins with  
649 atypical disulfide bond pattern characterized in *Caenorhabditis elegans* by comparative  
650 sequence analysis and homology modeling. *Genome Res* 8, 348–353.  
651 <https://doi.org/10.1101/gr.8.4.348>.
- 652 31. Murphy, C.T., and Hu, P.J. (2013). Insulin/insulin-like growth factor signaling in *C. elegans*.  
653 *WormBook*, 1–43. <https://doi.org/10.1895/wormbook.1.164.1>.
- 654 32. Pierce, S.B., Costa, M., Wisotzkey, R., Devadhar, S., Homburger, S.A., Buchman, A.R.,  
655 Ferguson, K.C., Heller, J., Platt, D.M., Pasquinelli, A.A., et al. (2001). Regulation of DAF-2  
656 receptor signaling by human insulin and *ins-1*, a member of the unusually large and diverse  
657 *C. elegans* insulin gene family. *Genes Dev* 15, 672–686.  
658 <https://doi.org/10.1101/gad.867301>.
- 659 33. Zheng, S., Chiu, H., Boudreau, J., Papanicolaou, T., Bendena, W., and Chin-Sang, I.  
660 (2018). A functional study of all 40 *Caenorhabditis elegans* insulin-like peptides. *J Biol*  
661 *Chem* 293, 16912–16922. <https://doi.org/10.1074/jbc.RA118.004542>.
- 662 34. Aurelio, O., Hall, D.H., and Hobert, O. (2002). Immunoglobulin-domain proteins required for  
663 maintenance of ventral nerve cord organization. *Science* 295, 686–690.  
664 <https://doi.org/10.1126/science.1066642>.
- 665 35. Hutter, H. (2019). Formation of longitudinal axon pathways in *Caenorhabditis elegans*.  
666 *Semin Cell Dev Biol* 85, 60–70. <https://doi.org/10.1016/j.semcd.2017.11.015>.
- 667 36. Roed, N.K., Viola, C.M., Kristensen, O., Schluckebier, G., Norrman, M., Sajid, W., Wade,  
668 J.D., Andersen, A.S., Kristensen, C., Ganderton, T.R., et al. (2018). Structures of insect  
669 Imp-L2 suggest an alternative strategy for regulating the bioavailability of insulin-like  
670 hormones. *Nat Commun* 9, 3860. <https://doi.org/10.1038/s41467-018-06192-3>.
- 671 37. Menting, J.G., Whittaker, J., Margetts, M.B., Whittaker, L.J., Kong, G.K.-W., Smith, B.J.,  
672 Watson, C.J., Záková, L., Kletvíková, E., Jiráček, J., et al. (2013). How insulin engages its  
673 primary binding site on the insulin receptor. *Nature* 493, 241–245.  
674 <https://doi.org/10.1038/nature11781>.
- 675 38. Uchikawa, E., Choi, E., Shang, G., Yu, H., and Bai, X.-C. (2019). Activation mechanism of  
676 the insulin receptor revealed by cryo-EM structure of the fully liganded receptor-ligand  
677 complex. *eLife* 8, e48630. <https://doi.org/10.7554/eLife.48630>.



- 678 39. Patapoutian, A., and Reichardt, L.F. (2001). Trk receptors: mediators of neurotrophin action.  
679 *Curr Opin Neurobiol* 11, 272–280. [https://doi.org/10.1016/s0959-4388\(00\)00208-7](https://doi.org/10.1016/s0959-4388(00)00208-7).
- 680 40. Sun, P.D., and Davies, D.R. (1995). The cystine-knot growth-factor superfamily. *Annu Rev*  
681 *Biophys Biomol Struct* 24, 269–291. <https://doi.org/10.1146/annurev.bb.24.060195.001413>.
- 682 41. Vozdek, R., Long, Y., and Ma, D.K. (2018). The receptor tyrosine kinase HIR-1 coordinates  
683 HIF-independent responses to hypoxia and extracellular matrix injury. *Sci Signal* 11,  
684 eaat0138. <https://doi.org/10.1126/scisignal.aat0138>.
- 685 42. Schlessinger, J., Plotnikov, A.N., Ibrahimi, O.A., Eliseenkova, A.V., Yeh, B.K., Yayon, A.,  
686 Linhardt, R.J., and Mohammadi, M. (2000). Crystal structure of a ternary FGF-FGFR-  
687 heparin complex reveals a dual role for heparin in FGFR binding and dimerization. *Mol Cell*  
688 6, 743–750. [https://doi.org/10.1016/s1097-2765\(00\)00073-3](https://doi.org/10.1016/s1097-2765(00)00073-3).
- 689 43. Messina, A., Pulli, K., Santini, S., Acierno, J., Käsäkoski, J., Cassatella, D., Xu, C., Casoni,  
690 F., Malone, S.A., Ternier, G., et al. (2020). Neuron-Derived Neurotrophic Factor Is Mutated  
691 in Congenital Hypogonadotropic Hypogonadism. *Am J Hum Genet* 106, 58–70.  
692 <https://doi.org/10.1016/j.ajhg.2019.12.003>.
- 693 44. Pitteloud, N., Acierno, J.S., Meysing, A., Eliseenkova, A.V., Ma, J., Ibrahimi, O.A., Metzger,  
694 D.L., Hayes, F.J., Dwyer, A.A., Hughes, V.A., et al. (2006). Mutations in fibroblast growth  
695 factor receptor 1 cause both Kallmann syndrome and normosmic idiopathic  
696 hypogonadotropic hypogonadism. *Proc Natl Acad Sci U S A* 103, 6281–6286.  
697 <https://doi.org/10.1073/pnas.0600962103>.
- 698 45. Cheng, S., Park, Y., Kurlito, J.D., Jeon, M., Zinn, K., Thornton, J.W., and Özkan, E. (2019).  
699 Family of neural wiring receptors in bilaterians defined by phylogenetic, biochemical, and  
700 structural evidence. *Proc Natl Acad Sci U S A* 116, 9837–9842.  
701 <https://doi.org/10.1073/pnas.1818631116>.
- 702 46. Lobb-Rabe, M., Nawrocka, W.I., Carrillo, R.A., and Özkan, E. (2023). Neuronal wiring  
703 receptors Dprs and DIPs are GPI anchored and this modification contributes to their cell  
704 surface organization. Preprint at bioRxiv, <https://doi.org/10.1101/2023.03.02.530872>  
705 <https://doi.org/10.1101/2023.03.02.530872>.
- 706 47. Baumgartner, S., Littleton, J.T., Broadie, K., Bhat, M.A., Harbecke, R., Lengyel, J.A.,  
707 Chiquet-Ehrismann, R., Prokop, A., and Bellen, H.J. (1996). A *Drosophila* neurexin is  
708 required for septate junction and blood-nerve barrier formation and function. *Cell* 87, 1059–  
709 1068. [https://doi.org/10.1016/s0092-8674\(00\)81800-0](https://doi.org/10.1016/s0092-8674(00)81800-0).
- 710 48. Meng, L., and Yan, D. (2020). NLR-1/CASPR Anchors F-Actin to Promote Gap Junction  
711 Formation. *Dev Cell* 55, 574-587.e3. <https://doi.org/10.1016/j.devcel.2020.10.020>.
- 712 49. Einheber, S., Zanazzi, G., Ching, W., Scherer, S., Milner, T.A., Peles, E., and Salzer, J.L.  
713 (1997). The axonal membrane protein Caspr, a homologue of neurexin IV, is a component  
714 of the septate-like paranodal junctions that assemble during myelination. *J Cell Biol* 139,  
715 1495–1506. <https://doi.org/10.1083/jcb.139.6.1495>.
- 716 50. Poliak, S., Gollan, L., Martinez, R., Custer, A., Einheber, S., Salzer, J.L., Trimmer, J.S.,  
717 Shrager, P., and Peles, E. (1999). Caspr2, a new member of the neurexin superfamily, is  
718 localized at the juxtaparanodes of myelinated axons and associates with K<sup>+</sup> channels.  
719 *Neuron* 24, 1037–1047. [https://doi.org/10.1016/s0896-6273\(00\)81049-1](https://doi.org/10.1016/s0896-6273(00)81049-1).

- 720 51. Anderson, G.R., Galfin, T., Xu, W., Aoto, J., Malenka, R.C., and Südhof, T.C. (2012).  
721 Candidate autism gene screen identifies critical role for cell-adhesion molecule CASPR2 in  
722 dendritic arborization and spine development. *Proc Natl Acad Sci U S A* *109*, 18120–18125.  
723 <https://doi.org/10.1073/pnas.1216398109>.
- 724 52. Varea, O., Martin-de-Saavedra, M.D., Kopeikina, K.J., Schürmann, B., Fleming, H.J.,  
725 Fawcett-Patel, J.M., Bach, A., Jang, S., Peles, E., Kim, E., et al. (2015). Synaptic  
726 abnormalities and cytoplasmic glutamate receptor aggregates in contactin associated  
727 protein-like 2/Caspr2 knockout neurons. *Proc Natl Acad Sci U S A* *112*, 6176–6181.  
728 <https://doi.org/10.1073/pnas.1423205112>.
- 729 53. Kaufmann, N., DeProto, J., Ranjan, R., Wan, H., and Van Vactor, D. (2002). *Drosophila*  
730 liprin-alpha and the receptor phosphatase Dlar control synapse morphogenesis. *Neuron* *34*,  
731 27–38. [https://doi.org/10.1016/s0896-6273\(02\)00643-8](https://doi.org/10.1016/s0896-6273(02)00643-8).
- 732 54. Johnson, K.G., Tenney, A.P., Ghose, A., Duckworth, A.M., Higashi, M.E., Parfitt, K., Marcu,  
733 O., Heslip, T.R., Marsh, J.L., Schwarz, T.L., et al. (2006). The HSPGs Syndecan and  
734 Dallylike bind the receptor phosphatase LAR and exert distinct effects on synaptic  
735 development. *Neuron* *49*, 517–531. <https://doi.org/10.1016/j.neuron.2006.01.026>.
- 736 55. Carrillo, R.A., Özkan, E., Menon, K.P., Nagarkar-Jaiswal, S., Lee, P.-T., Jeon, M.,  
737 Birnbaum, M.E., Bellen, H.J., Garcia, K.C., and Zinn, K. (2015). Control of Synaptic  
738 Connectivity by a Network of *Drosophila* IgSF Cell Surface Proteins. *Cell* *163*, 1770–1782.  
739 <https://doi.org/10.1016/j.cell.2015.11.022>.
- 740 56. Broadbent, I.D., and Pettitt, J. (2002). The *C. elegans* hmr-1 gene can encode a neuronal  
741 classic cadherin involved in the regulation of axon fasciculation. *Curr Biol* *12*, 59–63.  
742 [https://doi.org/10.1016/s0960-9822\(01\)00624-8](https://doi.org/10.1016/s0960-9822(01)00624-8).
- 743 57. Barnes, K.M., Fan, L., Moyle, M.W., Brittin, C.A., Xu, Y., Colón-Ramos, D.A., Santella, A.,  
744 and Bao, Z. (2020). Cadherin preserves cohesion across involuting tissues during *C.*  
745 *elegans* neurulation. *eLife* *9*, e58626. <https://doi.org/10.7554/eLife.58626>.
- 746 58. Cebul, E.R., Marivin, A., Wexler, L.R., Perrat, P.N., Bénard, C.Y., Garcia-Marcos, M., and  
747 Heiman, M.G. (2024). SAX-7/L1CAM acts with the adherens junction proteins MAGI-1,  
748 HMR-1/Cadherin, and AFD-1/Afadin to promote glial-mediated dendrite extension. Preprint  
749 at bioRxiv, <https://doi.org/10.1101/2024.01.11.575259>  
750 <https://doi.org/10.1101/2024.01.11.575259>.
- 751 59. Yonekura, S., Xu, L., Ting, C.-Y., and Lee, C.-H. (2007). Adhesive but not signaling activity  
752 of *Drosophila* N-cadherin is essential for target selection of photoreceptor afferents. *Dev Biol*  
753 *304*, 759–770. <https://doi.org/10.1016/j.ydbio.2007.01.030>.
- 754 60. Pecot, M.Y., Tadros, W., Nern, A., Bader, M., Chen, Y., and Zipursky, S.L. (2013). Multiple  
755 interactions control synaptic layer specificity in the *Drosophila* visual system. *Neuron* *77*,  
756 299–310. <https://doi.org/10.1016/j.neuron.2012.11.007>.
- 757 61. Mirdita, M., Schütze, K., Moriwaki, Y., Heo, L., Ovchinnikov, S., and Steinegger, M. (2022).  
758 ColabFold: making protein folding accessible to all. *Nat Methods* *19*, 679–682.  
759 <https://doi.org/10.1038/s41592-022-01488-1>.
- 760 62. Evans, R., O'Neill, M., Pritzel, A., Antropova, N., Senior, A., Green, T., Žídek, A., Bates, R.,  
761 Blackwell, S., Yim, J., et al. (2022). Protein complex prediction with AlphaFold-Multimer.  
762 Preprint at bioRxiv, <https://doi.org/10.1101/2021.10.04.463034>



- 763 <https://doi.org/10.1101/2021.10.04.463034>.
- 764 63. Schöneberg, T., and Prömel, S. (2019). Latrophilins and Teneurins in Invertebrates: No  
765 Love for Each Other? *Front Neurosci* 13, 154. <https://doi.org/10.3389/fnins.2019.00154>.
- 766 64. Carmona-Rosas, G., Li, J., Smith, J.J., Cheng, S., Baltrusaitis, E., Nawrocka, W.I., Zhao,  
767 M., Kratsios, P., Araç, D., and Özkan, E. (2023). Structural basis and functional roles for  
768 Toll-like receptor binding to Latrophilin adhesion-GPCR in embryo development. Preprint at  
769 bioRxiv, <https://doi.org/10.1101/2023.05.04.539414>  
770 <https://doi.org/10.1101/2023.05.04.539414>.
- 771 65. Südhof, T.C. (2017). Synaptic Neurexin Complexes: A Molecular Code for the Logic of  
772 Neural Circuits. *Cell* 171, 745–769. <https://doi.org/10.1016/j.cell.2017.10.024>.
- 773 66. Hu, Z., Hom, S., Kudze, T., Tong, X.-J., Choi, S., Aramuni, G., Zhang, W., and Kaplan, J.M.  
774 (2012). Neurexin and neuroligin mediate retrograde synaptic inhibition in *C. elegans*.  
775 *Science* 337, 980–984. <https://doi.org/10.1126/science.1224896>.
- 776 67. Ichtchenko, K., Hata, Y., Nguyen, T., Ullrich, B., Missler, M., Moomaw, C., and Südhof, T.C.  
777 (1995). Neuroligin 1: a splice site-specific ligand for beta-neurexins. *Cell* 81, 435–443.  
778 [https://doi.org/10.1016/0092-8674\(95\)90396-8](https://doi.org/10.1016/0092-8674(95)90396-8).
- 779 68. Araç, D., Boucard, A.A., Özkan, E., Strop, P., Newell, E., Südhof, T.C., and Brunger, A.T.  
780 (2007). Structures of neuroligin-1 and the neuroligin-1/neurexin-1 beta complex reveal  
781 specific protein-protein and protein-Ca<sup>2+</sup> interactions. *Neuron* 56, 992–1003.  
782 <https://doi.org/10.1016/j.neuron.2007.12.002>.
- 783 69. Comoletti, D., Flynn, R., Jennings, L.L., Chubykin, A., Matsumura, T., Hasegawa, H.,  
784 Südhof, T.C., and Taylor, P. (2003). Characterization of the interaction of a recombinant  
785 soluble neuroligin-1 with neurexin-1beta. *J Biol Chem* 278, 50497–50505.  
786 <https://doi.org/10.1074/jbc.M306803200>.
- 787 70. Ko, J., Zhang, C., Arac, D., Boucard, A.A., Brunger, A.T., and Südhof, T.C. (2009).  
788 Neuroligin-1 performs neurexin-dependent and neurexin-independent functions in synapse  
789 validation. *EMBO J* 28, 3244–3255. <https://doi.org/10.1038/emboj.2009.249>.
- 790 71. Maro, G.S., Gao, S., Olechwier, A.M., Hung, W.L., Liu, M., Özkan, E., Zhen, M., and Shen,  
791 K. (2015). MADD-4/Punctin and Neurexin Organize *C. elegans* GABAergic Postsynapses  
792 through Neuroligin. *Neuron* 86, 1420–1432. <https://doi.org/10.1016/j.neuron.2015.05.015>.
- 793 72. Zhang, P., Lu, H., Peixoto, R.T., Pines, M.K., Ge, Y., Oku, S., Siddiqui, T.J., Xie, Y., Wu, W.,  
794 Archer-Hartmann, S., et al. (2018). Heparan Sulfate Organizes Neuronal Synapses through  
795 Neurexin Partnerships. *Cell* 174, 1450-1464.e23. <https://doi.org/10.1016/j.cell.2018.07.002>.
- 796 73. Schweke, H., Pacesa, M., Levin, T., Goverde, C.A., Kumar, P., Duhoo, Y., Dornfeld, L.J.,  
797 Dubreuil, B., Georgeon, S., Ovchinnikov, S., et al. (2024). An atlas of protein homo-  
798 oligomerization across domains of life. *Cell* 187, 999-1010.e15.  
799 <https://doi.org/10.1016/j.cell.2024.01.022>.
- 800 74. Sanes, J.R., and Zipursky, S.L. (2020). Synaptic Specificity, Recognition Molecules, and  
801 Assembly of Neural Circuits. *Cell* 181, 536–556. <https://doi.org/10.1016/j.cell.2020.04.008>.
- 802 75. Varshney, L.R., Chen, B.L., Paniagua, E., Hall, D.H., and Chklovskii, D.B. (2011). Structural  
803 properties of the *Caenorhabditis elegans* neuronal network. *PLoS Comput Biol* 7,

- 804 e1001066. <https://doi.org/10.1371/journal.pcbi.1001066>.
- 805 76. Taylor, S.R., Santpere, G., Weinreb, A., Barrett, A., Reilly, M.B., Xu, C., Varol, E.,  
806 Oikonomou, P., Glenwinkel, L., McWhirter, R., et al. (2021). Molecular topography of an  
807 entire nervous system. *Cell* 184, 4329-4347.e23. <https://doi.org/10.1016/j.cell.2021.06.023>.
- 808 77. Asan, A., Raiders, S.A., and Priess, J.R. (2016). Morphogenesis of the *C. elegans* Intestine  
809 Involves Axon Guidance Genes. *PLoS Genet* 12, e1005950.  
810 <https://doi.org/10.1371/journal.pgen.1005950>.
- 811 78. Dong, B., Moseley-Aldredge, M., Schwieterman, A.A., Donelson, C.J., McMurry, J.L.,  
812 Hudson, M.L., and Chen, L. (2016). EFN-4 functions in LAD-2-mediated axon guidance in  
813 *Caenorhabditis elegans*. *Development* 143, 1182–1191. <https://doi.org/10.1242/dev.128934>.
- 814 79. Wang, X., Zhang, W., Cheever, T., Schwarz, V., Opperman, K., Hutter, H., Koepf, D., and  
815 Chen, L. (2008). The *C. elegans* L1CAM homologue LAD-2 functions as a coreceptor in  
816 MAB-20/Sema2 mediated axon guidance. *J Cell Biol* 180, 233–246.  
817 <https://doi.org/10.1083/jcb.200704178>.
- 818 80. Nakao, F., Hudson, M.L., Suzuki, M., Peckler, Z., Kurokawa, R., Liu, Z., Gengyo-Ando, K.,  
819 Nukazuka, A., Fujii, T., Suto, F., et al. (2007). The PLEXIN PLX-2 and the ephrin EFN-4  
820 have distinct roles in MAB-20/Semaphorin 2A signaling in *Caenorhabditis elegans*  
821 morphogenesis. *Genetics* 176, 1591–1607. <https://doi.org/10.1534/genetics.106.067116>.
- 822 81. Hahn, A.C., and Emmons, S.W. (2003). The roles of an ephrin and a semaphorin in  
823 patterning cell-cell contacts in *C. elegans* sensory organ development. *Dev Biol* 256, 379–  
824 388. [https://doi.org/10.1016/s0012-1606\(02\)00129-x](https://doi.org/10.1016/s0012-1606(02)00129-x).
- 825 82. Ikegami, R., Zheng, H., Ong, S.-H., and Culotti, J. (2004). Integration of semaphorin-  
826 2A/MAB-20, ephrin-4, and UNC-129 TGF-beta signaling pathways regulates sorting of  
827 distinct sensory rays in *C. elegans*. *Dev Cell* 6, 383–395. [https://doi.org/10.1016/s1534-5807\(04\)00057-7](https://doi.org/10.1016/s1534-5807(04)00057-7).
- 829 83. Jaaro, H., Beck, G., Conticello, S.G., and Fainzilber, M. (2001). Evolving better brains: a  
830 need for neurotrophins? *Trends Neurosci* 24, 79–85. [https://doi.org/10.1016/s0166-2236\(00\)01690-8](https://doi.org/10.1016/s0166-2236(00)01690-8).
- 832 84. Wiesmann, C., Ultsch, M.H., Bass, S.H., and de Vos, A.M. (1999). Crystal structure of nerve  
833 growth factor in complex with the ligand-binding domain of the TrkA receptor. *Nature* 401,  
834 184–188. <https://doi.org/10.1038/43705>.
- 835 85. Banfield, M.J., Naylor, R.L., Robertson, A.G., Allen, S.J., Dawbarn, D., and Brady, R.L.  
836 (2001). Specificity in Trk receptor:neurotrophin interactions: the crystal structure of TrkB-d5  
837 in complex with neurotrophin-4/5. *Structure* 9, 1191–1199. [https://doi.org/10.1016/s0969-2126\(01\)00681-5](https://doi.org/10.1016/s0969-2126(01)00681-5).
- 839 86. Wehrman, T., He, X., Raab, B., Dukipatti, A., Blau, H., and Garcia, K.C. (2007). Structural  
840 and mechanistic insights into nerve growth factor interactions with the TrkA and p75  
841 receptors. *Neuron* 53, 25–38. <https://doi.org/10.1016/j.neuron.2006.09.034>.
- 842 87. Yang, S., Wu, X., Daoutidou, E.I., Zhang, Y., Shimell, M., Chuang, K.-H., Peterson, A.J.,  
843 O'Connor, M.B., and Zheng, X. (2022). The NDNF-like factor Nord is a Hedgehog-induced  
844 extracellular BMP modulator that regulates *Drosophila* wing patterning and growth. *eLife* 11,  
845 e73357. <https://doi.org/10.7554/eLife.73357>.

- 846 88. Akiyama, T., Seidel, C.W., and Gibson, M.C. (2022). The feedback regulator Nord controls  
847 Dpp/BMP signaling via extracellular interaction with Dally in the *Drosophila* wing. *Dev Biol*  
848 488, 91–103. <https://doi.org/10.1016/j.ydbio.2022.05.008>.
- 849 89. Letunic, I., and Bork, P. (2018). 20 years of the SMART protein domain annotation resource.  
850 *Nucleic Acids Res* 46, D493–D496. <https://doi.org/10.1093/nar/gkx922>.
- 851 90. Wilson, D., Pethica, R., Zhou, Y., Talbot, C., Vogel, C., Madera, M., Chothia, C., and  
852 Gough, J. (2009). SUPERFAMILY--sophisticated comparative genomics, data mining,  
853 visualization and phylogeny. *Nucleic Acids Res* 37, D380–386.  
854 <https://doi.org/10.1093/nar/gkn762>.
- 855 91. Käll, L., Krogh, A., and Sonnhammer, E.L.L. (2004). A combined transmembrane topology  
856 and signal peptide prediction method. *J Mol Biol* 338, 1027–1036.  
857 <https://doi.org/10.1016/j.jmb.2004.03.016>.
- 858 92. Pierleoni, A., Martelli, P.L., and Casadio, R. (2008). PredGPI: a GPI-anchor predictor. *BMC*  
859 *Bioinformatics* 9, 392. <https://doi.org/10.1186/1471-2105-9-392>.
- 860 93. Gíslason, M.H., Nielsen, H., Almagro Armenteros, J.J., and Johansen, A.R. (2021).  
861 Prediction of GPI-anchored proteins with pointer neural networks. *Curr Res Biotechnol* 3, 6–  
862 13. <https://doi.org/10.1016/j.crbiot.2021.01.001>.
- 863 94. Varadi, M., Anyango, S., Deshpande, M., Nair, S., Natassia, C., Yordanova, G., Yuan, D.,  
864 Stroe, O., Wood, G., Laydon, A., et al. (2022). AlphaFold Protein Structure Database:  
865 massively expanding the structural coverage of protein-sequence space with high-accuracy  
866 models. *Nucleic Acids Res* 50, D439–D444. <https://doi.org/10.1093/nar/gkab1061>.
- 867 95. Potter, S.C., Luciani, A., Eddy, S.R., Park, Y., Lopez, R., and Finn, R.D. (2018). HMMER  
868 web server: 2018 update. *Nucleic Acids Res* 46, W200–W204.  
869 <https://doi.org/10.1093/nar/gky448>.
- 870 96. Cheng, S., Seven, A.B., Wang, J., Skiniotis, G., and Özkan, E. (2016). Conformational  
871 Plasticity in the Transsynaptic Neurexin-Cerebellin-Glutamate Receptor Adhesion Complex.  
872 *Structure* 24, 2163–2173. <https://doi.org/10.1016/j.str.2016.11.004>.
- 873 97. Kabsch, W. (2010). XDS. *Acta Crystallogr D Biol Crystallogr* 66, 125–132.  
874 <https://doi.org/10.1107/S0907444909047337>.
- 875 98. McCoy, A.J., Grosse-Kunstleve, R.W., Adams, P.D., Winn, M.D., Storoni, L.C., and Read,  
876 R.J. (2007). *Phaser* crystallographic software. *J Appl Crystallogr* 40, 658–674.  
877 <https://doi.org/10.1107/S0021889807021206>.
- 878 99. Liebschner, D., Afonine, P.V., Baker, M.L., Bunkóczi, G., Chen, V.B., Croll, T.I., Hintze, B.,  
879 Hung, L.W., Jain, S., McCoy, A.J., et al. (2019). Macromolecular structure determination  
880 using X-rays, neutrons and electrons: recent developments in *Phenix*. *Acta Crystallogr D*  
881 *Struct Biol* 75, 861–877. <https://doi.org/10.1107/S2059798319011471>.
- 882 100. Afonine, P.V., Grosse-Kunstleve, R.W., Echols, N., Headd, J.J., Moriarty, N.W.,  
883 Mustyakimov, M., Terwilliger, T.C., Urzhumtsev, A., Zwart, P.H., and Adams, P.D. (2012).  
884 Towards automated crystallographic structure refinement with *phenix.refine*. *Acta*  
885 *Crystallogr D Biol Crystallogr* 68, 352–367. <https://doi.org/10.1107/S0907444912001308>.
- 886 101. Emsley, P., Lohkamp, B., Scott, W.G., and Cowtan, K. (2010). Features and

887 development of *Coot*. *Acta Crystallogr D Biol Crystallogr* 66, 486–501.  
888 <https://doi.org/10.1107/S0907444910007493>.

889 102. Chen, V.B., Arendall, W.B., Headd, J.J., Keedy, D.A., Immormino, R.M., Kapral, G.J.,  
890 Murray, L.W., Richardson, J.S., and Richardson, D.C. (2010). *MolProbity*: all-atom structure  
891 validation for macromolecular crystallography. *Acta Crystallogr D Biol Crystallogr* 66, 12–21.  
892 <https://doi.org/10.1107/S0907444909042073>.

893

894

## 895     **METHODS**

### 896     **Selection of Ectodomains**

897     We collected names of genes annotated to have selected domains from *SMART*<sup>89</sup> and  
898     *SUPERFAMILY*<sup>90</sup> databases in the *C. elegans* genome. Transcripts for these genes were  
899     identified in the WS252 release of the *C. elegans* genome, and analyzed using *phobius* for signal  
900     peptide and transmembrane domains.<sup>91</sup> The identified ectodomains were written into Genbank-  
901     formatted files for bait and prey plasmids for cloning and/or gene synthesis. The bioinformatic  
902     pipeline described above was performed using tools available in Bioperl modules. Proteins that  
903     have no discernable transmembrane domains were also run on the PredGPI<sup>92</sup> server  
904     (<http://gpcr.biocomp.unibo.it/predgpi/>) to assess whether they may be GPI-anchored; we removed  
905     the C-terminal GPI anchoring sequences for those proteins with predicted GPI-anchors.  
906     Predictions were repeated with the recently released NetGPI<sup>93</sup> to update **Table S1**.

907     Following curation of ectodomain sequences, included in **Table S1**, we re-analyzed domain  
908     compositions using updated tools and AlphaFold predictions,<sup>94</sup> which became available as we  
909     prepared the manuscript for publication. Based on the results from these tools, we decided not to  
910     distinguish EGF domains from WR1 domains (SMART SM00289; Interpro IPR006150), EB  
911     modules (Pfam PF01683) and Lustrin-type Cys-rich domains (Pfam PF14625; Interpro  
912     IPR028150), which were previously defined using sequence alignments. We observed that  
913     domain prediction tools such as *SMART* and *hmmscan*<sup>95</sup> repeatedly gave overlapping predictions  
914     for these families, and structure predictions showed strong similarities and a continuum of  
915     elaborations above basic features, making a rigid distinction between these folds difficult. Future  
916     work using experimentally determined structures, predictions and sequence alignments will be  
917     necessary to carefully classify similar Cys-rich small domains into better-defined categories.

### 918     **Ectodomain Expression Library Construction and Protein Expression**

919     To facilitate protein expression, we built new ECIA vectors carrying the strong constitutively active  
920     Actin 5C promoter rather than the inducible metallothionein promoter on pECIA2 and pECIA14  
921     described in Özkan *et al.*<sup>4</sup> Briefly, the multiple cloning site (MCS) region of pACTIN-SV<sup>17</sup> was  
922     replaced by a BiP signal sequence followed by the cassette attB1-MCS-attB2-3C-Fc-V5 tag-His<sub>6</sub>

923 (3C: HRV 3C Protease site) to generate the bait vector pECIA75, while the replacement of the  
924 MCS of pACTIN-SV by BiP-attB1-MCS-attB2-3C-COMP-AP-FLAG-His6 (COMP: pentameric  
925 coiled coil from rat COMP; AP: human placental alkaline phosphatase) resulted in the prey vector  
926 pECIA76.

927 To construct the expression library for the proteins of interest listed in Table S1, the ectodomains  
928 of 16 proteins from our lab collection were subcloned into the MCS of the new ECIA vectors. We  
929 also purchased a *C. elegans* ORF library from GE Healthcare and found 107 proteins in Table S1  
930 from the 12611 clones of the ORF library. However, only 63 (including 5 with mutation(s) or  
931 intron(s) that were corrected in cloning) were successfully subcloned while the remaining 44  
932 clones from the clone collection proved to be wrong or empty vectors. Through RT-PCR, 9 were  
933 amplified from a *C.elegans* N2 mRNA pool (gift from Kang Shen at Stanford). The left 288 were  
934 synthesized by GenScript.

935 Every bait or prey construct was individually expressed using transient transfection of *Drosophila*  
936 Schneider 2 (S2) cells in Schneider's medium with 1.8 g/L L-Glutamine (Gibco, 21720024) with  
937 10% Fetal Bovine Serum, 50 units/ml Penicillin, and 50 µg/ml Streptomycin. Briefly, 10 mL of S2  
938 cells at 1.8 million per mL were seeded in T75 flasks and incubated at 28°C overnight. The cells  
939 were transfected transiently next day with 5 µg of each plasmid using TransIT®-Insect  
940 Transfection Reagent (Mirus, MIR 6104) following manufacturer's manuals. Conditioned media  
941 were collected 4 days after transfection. Protease inhibitors (Sigma, P8849) and 0.02% NaN<sub>3</sub>  
942 were added to harvested media before storage at 4°C in 15 mL conical tubes.

943 All bait and prey samples collected were run on SDS-PAGE gels, blotted and probed with mouse  
944 THE™ His Tag Antibody [iFluor 488] (GenScript, A01800) for assessing protein expression. Bio-  
945 Rad ChemiDoc Imaging System was used to quantitate the bait and prey samples based on the  
946 reference band of 0.1 µM rat His<sub>6</sub>-tagged GluD2 ectodomain (ATD+LBD)<sup>96</sup> on each blot. Overall,  
947 we observed expression as high as ~0.31 µM (LRON-3-Fc) in conditioned media. The lowest  
948 protein concentration we could detect and measure was ~0.45 nM, for R09H10.5-AP<sub>5</sub>. Expression  
949 for 23% of the samples could not be detected. Relative expression levels are reported in **Table**  
950 **S1**.



## 951 **Extracellular Interactome Assay (ECIA)**

952 Clear Nunc 384-well MaxiSorp plates (Thermo Scientific, 464718) were coated with 20  $\mu$ l 5  $\mu$ g/mL  
953 Protein A (Genscript, Z02201) in 100 mM sodium bicarbonate pH 9.6 at 4°C overnight. Excess  
954 protein A was discarded, and the coated plates were blocked with 90  $\mu$ l 10% SuperBlock™ T20  
955 (PBS) Blocking Buffer (ThermoFisher, 37516) in PBS at 500x rpm for 3 hours at room temperature.  
956 The blocking buffer was then removed, and the plates were washed three times with 90  $\mu$ l PBST  
957 (PBS + 0.1% Tween 20) using a microplate washer (BioTek). 20  $\mu$ l of medium containing a  
958 secreted Fc-fusion protein (bait) was added into wells of a single plate at 4°C with a shaking at  
959 500 rpm on a plate shaker overnight for bait capture. Next day, plates were blocked with 1%  
960 Bovine Serum Albumin (BSA) in PBS for three hours at room temperature while shaking at 500  
961 rpm, followed by three washes with 90  $\mu$ l of wash buffer (PBS with 1 mM CaCl<sub>2</sub>, 1 mM MgCl<sub>2</sub>, and  
962 0.1% BSA). This was followed by addition of 20  $\mu$ l of different medium containing secreted AP<sub>5</sub>-  
963 fusion proteins (prey) into each well of a plate using a Rainin BenchSmart 96-well multipipetter  
964 and incubation at room temperature while shaking at 500 rpm for 3 hours. The plates were then  
965 washed three times with 90  $\mu$ l of wash buffer. Finally, 50  $\mu$ l of BluePhos Phosphatase Substrate  
966 (KPL, 50-88-02) was added to each well using a Rainin BenchSmart 96-well multipipetter at room  
967 temperature. Absorbance at 650 nm was measured at 1 and 2 hours using a microplate reader  
968 and images of these 384-well plates were scanned.

## 969 **The contents of the large high-throughput screen data**

970 Each 384-well plate included four control measurements and 379 prey paired against one bait (+  
971 one prey, NAS-23, repeated as a control but not used in the analysis). The 379 unique  
972 ectodomains correspond to 374 genes, where some genes were represented by more than one  
973 constructs, such as the N- and C-terminal fragments of SLT-1 (see Table S1).

974 The large ECIA screen data has each pairwise heterotypic interaction tested twice, with each  
975 protein alternatively in the bait vs. prey configuration; this yielded two separate reports of  
976 interaction strength. Homotypic interactions were measured once.

## 977 **Analysis of ECIA Data: MaxEnt statistical model**

978 To assess the significance of interactions, we employ a maximum entropy network ensemble-

979 based technique<sup>19</sup> to construct a statistical model that captures the absorbance background.  
 980 Initially, we represent the experimental network by an  $n \times m$  matrix  $A$  and normalize it as  $An =$   
 981  $A/A_{max}$  (**Figure S2A**). Here, the rows and columns denote prey and bait, respectively, while  
 982 entries denote the normalized absorbance of each candidate protein-protein interaction (PPI). To  
 983 capture the random background given the observed row and column sums of  $An$ , we maximize  
 984 the entropy of a random network ensemble, denoted as  $S = -\sum_G P(G) \ln P(G)$ , subject to soft  
 985 constraints that preserve the average row and column sums of the normalized experimental data  
 986  $An$ . Here,  $G$  denotes random networks and  $P$  denotes the probability of  $G$ . With maximized  
 987 entropy, the model generates an ensemble with the broadest distribution of binary networks (a  
 988 matrix with only 0 and 1 entries) that on average replicates the row and column sums of  $An$ . The  
 989 average matrix of the  $P$  serves as the baseline expectation with the absence of any biological  
 990 information (Figure 1B). Each matrix entry in  $P$  representing the connection probability of a prey-  
 991 bait pair as  $p_{ij} = 1/(\alpha_i\beta_j + 1)$ . In practice, the parameters  $\alpha_i, \beta_j$  are iteratively determined to  
 992 preserve the mean total normalized absorbance of each prey  $k_i = \sum_j a_{ij}$  and bait  $k_j = \sum_i a_{ij}$  as

$$993 \quad \alpha_i = \frac{1}{k_i} \sum_j \frac{1}{\beta_j + 1/\alpha_i}$$

$$994 \quad \beta_j = \frac{1}{k_j} \sum_i \frac{1}{\alpha_i + 1/\beta_j}$$

995 where  $a_{ij}$  represents the elements in the normalized absorbance matrix  $An$ . Here we apply 100  
 996 iterations to ensure the convergence of  $\alpha_i$  and  $\beta_j$ . With these optimized  $\alpha_i$  ( $\beta_j$ ) for each row  
 997 (column), we test the self-consistency of the model by verifying the implication that all  $a_{ij}$  should  
 998 satisfy  $a_{ij} = 1/(1 + \alpha_i\beta_j)$ . However, upon using the optimized  $\alpha_i$  and  $\beta_j$ , we obtain sets of  $m$  ( $n$ )  
 999 different values of  $\alpha_i$  ( $\beta_j$ ) for each  $\alpha_i$  ( $\beta_j$ ), calculated as  $\{\alpha_i\} = (a_{ij}^{-1} - 1)/\beta_j \forall j$  and  $\{\beta_j\} =$   
 1000  $(a_{ij}^{-1} - 1)/\alpha_i \forall i$ . We observed small fluctuations of these  $\{\alpha_i\}$  and  $\{\beta_j\}$  around the optimized  
 1001 values, quantified as  $\sigma_{\alpha_i} = STD(\{\alpha_i\})$  and  $\sigma_{\beta_j} = STD(\{\beta_j\})$ . The standard deviation of  $p_{ij}$  is then

$$1002 \quad \text{calculated using error propagation as } \sigma_p = \sqrt{\left(\frac{\partial p}{\partial \alpha_i} \sigma_{\alpha_i}\right)^2 + \left(\frac{\partial p}{\partial \beta_j} \sigma_{\beta_j}\right)^2}. \sigma_p \text{ quantifies the systematic}$$

1003 error that emerges from the deviation of the experimental data from the statistical model. In

1004 principle, there is also statistical error in  $p_{ij}$  that can be calculated by  $\sigma_{p_{ij}} \propto p_{ij}(1 - p_{ij})$ . However,  
1005 we find that the systematic error dominates in this case, thus, the statistical error is ignored. z-  
1006 scores are used to identify potential signals that are significantly different from the baseline  
1007 expectation as  $z = \frac{An-P}{\sigma_P}$ .

1008 Although the z-score matrix can be asymmetric, we anticipate that a large fraction of the PPIs are  
1009 symmetric, meaning reciprocated signal in the two experimental directions ( $s \rightarrow t$  or  $t \rightarrow s$ ). Thus,  
1010 the reciprocal ratio of interactions works as a metric to reflect the precision of the experiment, akin  
1011 to a cross-validation scenario. In **Figures S2D-E**, we illustrate how the reciprocal ratio of  
1012 interactions varies with different z-score thresholds and unique PPIs. We assign z-score to each  
1013 PPI by symmetrizing z scores in both directions as  $z = (z_{A \rightarrow B} + z_{B \rightarrow A})/\sqrt{2}$  (**Table S2**). The scaling  
1014 factor  $\sqrt{2}$  ensures that the combined z-score remains a standard z-score, allowing for direct  
1015 comparison and interpretation. We use the reciprocal ratio to determine the ideal z-score  
1016 threshold to distinguish signal from background noise. Our analysis demonstrates that the  
1017 maximum reciprocal ratio of 0.67, corresponding to 145 unique PPIs, is achieved at a stringent  
1018 threshold of  $z = 12.2$ . Additionally, we observe that the reciprocal ratio fluctuates slightly  
1019 between 0.61 and 0.67 for z-scores between 8.4 and 33.6 (**Figure S2D**). As a result, we propose  
1020 an intermediate threshold of  $z = 8.4$ , which includes 185 unique PPIs (**Figure S2C, Table S3**).  
1021 Selecting an even lower threshold is expected to include more false positives as indicated by a  
1022 diminishing reciprocal ratio.

## 1023 **Network Analysis of ECIA Data and Communities**

1024 Network theory offers a particularly powerful framework for mining insight from measurements of  
1025 physical protein-protein interactions. Here, we conducted a network analysis of our ECIA dataset.

1026 *Community detection:* We identified communities in this PPI network using a multi-scale partition  
1027 algorithm,<sup>21</sup> which identifies node groupings of different sizes by random walks of various lengths.  
1028 The scale of the communities obtained by this approach is controlled by a hyperparameter tau  
1029 (resolution), analogous to the length of the walk. Smaller values of tau correspond to shorter walks,  
1030 which will on average end relatively close to where they begin. This results in the identification of

1031 relatively small communities. As the length of the walk ( $\tau$ ) increases, increasingly large  
1032 neighborhoods are reached, with the likelihood of remaining in any particular neighborhood of the  
1033 network as the walk proceeds determined by how insular the connectivity is within that  
1034 neighborhood. We used this method across 50-fold variation in  $\tau$  (0.1 to 5) to compute  
1035 community partitions at a variety of scales. For each protein, we recorded the union of all other  
1036 nodes that appear in the same community, across all choices of  $\tau$ . The subset of proteins  
1037 grouped in the same community across at least 25% of the  $\tau$  range and  $z_{\min}$  range are further  
1038 labeled as “canonical” community neighbors, and are made available in Table S4.

1039 Network analyses were performed using custom code written in Python 3.9, using NetworkX and  
1040 python-louvain (<https://github.com/taynaud/python-louvain>). Network visualization was performed  
1041 using NetworkX and Gephi. Code, data and output neighbor lists are available at  
1042 <https://github.com/mattrosen/ECIA-network-analysis>.

#### 1043 **Protein Expression and Purification for Interaction Validation**

1044 For crystallography and SPR experiments, proteins were produced using baculoviral infection of  
1045 *Trichoplusia ni* cells cultured in Insect-XPRESS (Lonza, BP12-730Q) or ESF 921 (Expression  
1046 Systems, 96-001) media. Ectodomains or smaller fragments of proteins were cloned into  
1047 baculoviral transfer vector pAcGP67 and baculoviruses viruses were generated with BestBac  
1048 linearized DNA (Expression systems, 91-002) using Sf9 cells cultured in Sf-900 III (Gibco,  
1049 12658019) with 10% FBS. The constructs were cloned with the addition of C-terminal biotin  
1050 acceptor peptide (for biotin capture on streptavidin-based SPR chips) followed by a hexahistidine  
1051 tag. The constructs used in crystallography were cloned with C-terminal hexahistidine tags only.  
1052 Proteins were purified from insect cell media using affinity chromatography with Ni-NTA agarose  
1053 resin (Pierce HisPur, 88223) followed by size-exclusion chromatography using Superdex 200  
1054 Increase or Superose 6 Increase 10/300 GL columns (Cytiva) in 10 mM HEPES, pH 7.2 or 7.4,  
1055 100 mM NaCl (HEPES-buffered saline; HBS). Proteins used in SPR experiments were usually  
1056 biotinylated using BirA ligase (Avidity, BirA500) and purified on size-exclusion columns to remove  
1057 free biotin.

#### 1058 **Surface Plasmon Resonance Experiments**

1059 SPR experiments were carried out using SA or CM5 sensor chips with Biacore T200 or 8K models  
1060 (Cytiva). Proteins were immobilized in HBSp+ (10 mM HEPES, 150 mM NaCl, 0.05% Tween 20),  
1061 pH 7.2 or 7.4 using biotin capture on SA chips, or random amine coupling on CM5 chips when  
1062 proteins were not tagged with a biotinylation sequence. Experiments were performed at 25°C, at  
1063 a flow rate of 30  $\mu$ l/min, with varying ligand immobilization levels (between ~ 500 RUs to 1200  
1064 RUs), association and dissociation times, running buffer, and regeneration conditions. Details of  
1065 the SPR experiments are listed in the **Table S6**. SPR sensorgrams and isotherms were plotted  
1066 using Prism version 10.

1067 For NDNF-1–EGL-15 SPR experiments (Figure 5E), 60 mL of S2 culture (in Schneider’s medium  
1068 supplemented with Insect media supplement, Sigma I7267, and no serum) was transiently  
1069 transfected with the Fc-tagged NDNF-1 (bait) expression plasmid, and conditioned medium was  
1070 collected three days post-transfection. Medium containing NDNF-1-Fc was dialyzed overnight  
1071 against HBS, pH 7.4, and was captured on Protein A SPR chips (Cytiva, 29127555) to validate  
1072 the NDNF-EGL-15 interaction, using purified EGL-15 ectodomain as analyte. We observed slow  
1073 dissociation of the NDNF-1-Fc from the SPR chip over several hours, resulting in a slow but  
1074 noticeable baseline drift.

1075 Except in cases where kinetics were too slow, we used the 1:1 Langmuir binding model for fitting  
1076 binding isotherms to acquire  $K_D$  values in Prism version 10. With slow kinetics, we fit sensorgrams  
1077 to kinetic models using Biacore’s BIAEvaluation software to acquire rate constants; we indicated  
1078 which kinetic model was used in the relevant figure legends.

### 1079 **Structure Determination for the ZIG-4–INS-6 complex**

1080 The ZIG-4–INS-6 complex was formed by co-expression using baculoviral expression of secreted  
1081 ZIG-4 and INS-6. Both proteins were C-terminally tagged with hexahistidine tags, which allowed  
1082 us to purify the complex from conditioned media using Ni-NTA Agarose resin. Complex was  
1083 further purified over a Superdex 200 10/300 Increase (Cytiva) size-exclusion chromatography  
1084 column in HBS. Purified complex was concentrated to 5 mg/ml, and screened for crystallization  
1085 using the sitting-drop vapor-diffusion method at 22°C.

1086 The ZIG-4–INS-6 complex crystallized in several conditions, which resulted in crystal structures

1087 resolved in three space groups. The tetragonal crystal form was grown in 0.1 M NaCl, 0.1 M  
1088 sodium cacodylate, pH 6.5, 2 M (NH<sub>4</sub>)<sub>2</sub>SO<sub>4</sub>. These crystals were cryo-protected in a solution  
1089 containing 0.1 M NaCl, 0.1 M sodium cacodylate, pH 6.4, 1.6 M (NH<sub>4</sub>)<sub>2</sub>SO<sub>4</sub> and 24% glycerol, and  
1090 diffracted to ~1.3 Å resolution. We also grew crystals The C-centered monoclinic crystals were  
1091 grown in 0.2 M sodium/potassium phosphate, 0.1 M bis-tris propane, pH 6.8, 28% PEG 3350.  
1092 These crystals were cryoprotected in 0.2 M sodium/potassium phosphate, 0.1 M bis-tris propane,  
1093 pH 6.8, 28% PEG 3350, and 20% glycerol, and diffracted to ~2.3 Å resolution. Finally, the primitive  
1094 monoclinic crystals were grown in 0.2 M sodium iodide, 0.1 M bis-tris propane, pH 6.5, 20% PEG  
1095 3350. These crystals were cryoprotected in 0.2 M sodium citrate, 0.1 M bis-tris propane, pH 6.5,  
1096 20% PEG 3350, and 25% glycerol, and diffracted to ~2.4 Å resolution.

1097 All crystallographic data were indexed, merged, and scaled using the *XDS* package.<sup>97</sup> Molecular  
1098 replacement was performed with *PHASER*<sup>98</sup> in the *PHENIX* package<sup>99</sup> using PDB ID: 6FEY  
1099 (ImpL2 + DILP5) as the molecular replacement model<sup>36</sup> with the tetragonal dataset. The refined  
1100 higher-resolution model was used for molecular replacement with the other two datasets.  
1101 *phenix.refine* was used to refine all models in reciprocal space and water placement,<sup>100</sup> and  
1102 *COOT* was used for model building and corrections in real space.<sup>101</sup> Model building and  
1103 refinement was guided by *MOLPROBITY* chemical validation tools within *PHENIX*.<sup>102</sup>

1104 The coordinates and structure factors for the ZIG-4–INS-6 complex are deposited at the Protein  
1105 Data Bank with the following accession codes: 8TK9 (tetragonal form), 8TKT (C-centered  
1106 monoclinic form), 8TKU (primitive monoclinic form). Crystallographic data collection and model  
1107 refinement statistics are in **Table S5**.

1108



1109 **FIGURE LEGENDS**

1110 **Figure 1. The *C. elegans* ectodomain collection and high-throughput interaction assay**  
1111 **design.**

1112 **A.** The distribution of secreted and membrane-anchored proteins in our *C. elegans* ectodomain  
1113 collection.

1114 **B, C.** The distribution of protein domains in the ectodomain collection.

1115 **D, E.** The design of the ECIA pipeline and data analysis.

1116 **F.** The expression levels of bait and prey proteins in the S2 cell culture media.  
1117

1118 **Figure 2. Interactions and the community structure of the extracellular interaction.**

1119 **A.** Network of moderate-confidence ( $z_{min} > 8.4$ ) protein-protein interactions ( $N = 185$ ) identified  
1120 via the maximum-entropy method; proteins are colored by community grouping.

1121 **B.** Network of community-community interactions. Only *connected communities* (communities  
1122 with at least one protein making at least one interaction outside the community;  $N = 14$ ) are  
1123 shown.

1124 **C.** List of proteins in each connected community.  
1125

1126 **Figure 3. Axon guidance receptors and cues interact with each other outside the known**  
1127 **cue-receptor axes.**

1128 **A.** Schematic of interactions from the high-throughput assay, where line thickness is scaled to  
1129 symmetrized MaxEnt z-scores (Figure 2). Interactions that were not previously known are shown  
1130 with red lines. The numbers next to the lines indicate z-scores.

1131 **B.** Interactions observed in the high-throughput assay are reproduced (see Figure S3 for more).  
1132 As expected, interactions observed with a bait-prey (Fc-AP) pair are also observed in the  
1133 reciprocal orientation, resulting in diagonally symmetrical assay results.

1134 **C-G.** ECIA can be used to identify domains required for novel interactions: The first two IG  
1135 domains of SAX-3 interact with the IPT domains 3 to 6 (C). SAX-3 IG domains also interact with  
1136 the second domain of EFN-4, as observed by ECIA (D) and size-exclusion chromatography (SEC)  
1137 (E). The interaction of MAB-20 with EFN-4 is mediated by the first domain (RBD) of EFN-4, as  
1138 observed by ECIA (F) and SEC (G). SDS-polyacrylamide gels show the presence of both  
1139 ectodomains in the complex fractions of SEC runs (E, G).

1140 **H.** Summary of interactions between the domains of the axon guidance receptors and cues. Black  
1141 arrows refer to interactions we observed but also previously characterized in other taxa.  
1142

1143 **Figure 4. ZIG-2, -3, -4 and -5 make up a family of insulin-binding IgSF proteins.**

1144 **A.** Pairwise sequence identities show that ZIG-2 to -5 are more closely related to each other and  
1145 to *Drosophila* ImpL2 than the rest of the ZIG family.

1146 **B.** ECIA for 22 insulin family members against ZIG-2 to -5. For expression levels of ZIGs and  
1147 insulins, see Figures S4C, S4D.

1148 **C.** ZIG-insulin interaction network inferred from the ECIA shown in B. The thickness of the  
1149 connecting lines reflects the absorbance values in B for each ZIG-insulin interaction.

1150 **D.** SPR sensorgrams for INS-1 and INS-6 binding to ZIG-5 and ZIG-4 immobilized on SPR chips.  
1151 Kinetic fits with estimated on- and off-rates and equilibrium constants are shown in Figure S4E.

1152 **E.** The structure of ZIG-4 (purple) bound to INS-6 (green) as observed in our tetragonal crystals.

1153 **F.** The structure of the ZIG-4–INS-6 complex strongly resembles that of *Drosophila* ImpL2 bound  
1154 to human IGF-1 (PDB ID: 6FF3).  
1155

1156 **Figure 5. Networks of interactions with growth factor-like molecules and receptors.**

1157 **A.** Network of interactions between cytokine- and growth factor-like molecules and receptors as  
1158 observed in our screen (Figure 2). Line thickness corresponds to the symmetrized z-scores for  
1159 each interaction. The numbers next to the lines indicate the z-score values.

1160 **B.** SPR sensorgrams for the interaction of TRK-1 with immobilized ZK856.6 and negative control  
1161 (hFGFR2 against ZK856.6).

1162 **C.** SPR sensorgrams for the interaction of B0222.11 with immobilized HIR-1 and negative control  
1163 (LET-756 against HIR-1). Kinetic fits and parameters are shown in Figure S5E.

1164 **D.** SPR sensorgrams and binding isotherms for the interaction of EGL-15 with immobilized LET-  
1165 756 in the presence or absence of 50 µg/mL (3.1 µM) heparin.

1166 **E.** SPR sensorgrams for the interaction of EGL-15 with immobilized Fc-tagged NDNF-1 and  
1167 negative control (HIR-1 against NDNF-1-Fc).  
1168

1169 **Figure 6. RIG-5 interacts with molecules with neuronal and synaptic functions.**

1170 **A.** Interactions of ZIG-8/Dpr and RIG-5/DIP according to our screen. Red and blue names  
1171 represent orthologs in *D. melanogaster* and mammals, respectively. Line thickness scales with  
1172 the symmetrized z-scores for each interaction. The numbers next to the lines indicate the z-score  
1173 values.

1174 **B-E.** SPR sensorgrams for interactions of RIG-5 with immobilized PTP-3 (B), NLR-1 (C),  
1175 T19D12.6 (D), and HMR-1 (E).

1176 **F.** Overlay of the ZIG-8–RIG-5 structure (PDB ID: 6ON9) (Cheng *et al.*, 2019) and AlphaFold-  
1177 multimer models for RIG-5 IG1-3+NLR-1 D6 and RIG-5 IG1-3+PTP-3 FN4-6. ZIG-8/Dpr binding  
1178 to RIG-5/DIP does not overlap with PTP-3 and NLR-1, which share a binding site on the RIG-5  
1179 IG2 domain. See Figure S6 for details of the AlphaFold-predicted interfaces. Predicted aligned  
1180 error (PAE) plots for AlphaFold predictions are shown for both RIG-5 (ECD)-PTP-3 (FN4-6) and  
1181 RIG-5 (ECD)-NLR-1 (D6) complexes.

1182 **G.** RIG-5 IG2 residues identified to interact with PTP-3 and NLR-1 in AlphaFold models.

1183 **H.** ECIA for RIG-5 ECD mutants against ZIG-8, PTP-3 and NLR-1 ECDs. Mutations in RIG-5 IG2  
1184 that break PTP-3 and NLR-1 binding do not affect ZIG-8 binding, which is known to happen  
1185 through the IG1 domain. The raw readout for the assay (absorbance at  $\lambda = 650$  nm) is noted in  
1186 each square. The homodimeric Rst interaction is a positive control.  
1187

1188 **Figure 7. AlphaFold predictions of extracellular protein complexes and chemical synapses**  
1189 **corresponding to PPIs.**

1190 **A.** ipTM (interface predicted Template Modelling) score values of AlphaFold-predicted complexes  
1191 from our interactome (blue) and random pairings of proteins (green).

1192 **B.** Size of the protein complex does not correlate with ipTM values. ECIA hits with previously  
1193 determined homologous structures (open blue circles) have the highest ipTM values on average.  
1194

1195 **SUPPLEMENTAL INFORMATION**

1196 **Figure S1. Domain collection, protein expression and network analysis.**

1197 **A.** Signal peptide and transmembrane helix analysis of the *C. elegans* proteome (WS252 release)  
1198 shows that 23% of proteins have predicted signal peptides, and 44% of proteins are either  
1199 membrane-anchored or secreted.

1200 **B-E.** Expression testing of *D. melanogaster* (blue) and *C. elegans* (green) ectodomains in S2 cells  
1201 using the Metallothionein (MT) and Actin 5C (Ac) promoters. Rst D1 refers to the first  
1202 immunoglobulin domain of Rst. For MT-driven expression, transiently transfected cells were  
1203 induced with 0.8 mM CuSO<sub>4</sub> at 16 hours post-transfection. All transfections were collected 88  
1204 hours post-transfection for western blotting using a mouse primary anti-His antibody (1:2000) and  
1205 an Alexa Fluor 488-coupled donkey anti-mouse IgG secondary antibody (1:5000). Overall, the  
1206 Actin 5C promoter results in higher expression, but not in every case.

1207 **F.** Network of 185 interactions detected with a cutoff of  $z_{\min} > 8.4$  drawn using the organic layout  
1208 algorithm in Cytoscape, where node size relates to node degree (see the legend), and the edge  
1209 thickness scales to  $z_{\min}$ .

1210 **G.** The degree distribution of all the interactions depicted in F.

1211

1212 **Figure S2. MaxEnt model to filter the experimental data.**

1213 **A.** The normalized experimental data  $A_n$ .

1214 **B.** The mean of the statistical background model  $P$ .

1215 **C.** The difference between  $A_n$  and  $P$ . PPIs with z-score above intermediate (orange) and stringent  
1216 (purple) thresholds are shown in matrix form. Reciprocal PPIs are marked with dots (•) and non-  
1217 reciprocal PPIs are marked with an 'x'.

1218 **D.** The reciprocal ratio of interactions as a function of the chosen threshold of z-scores. The  
1219 maximum reciprocal ratio is achieved with  $z = 12.2$ .

1220 **E.** The reciprocal ratio as a function of the number of unique edges identified. The shading  
1221 represents  $n \pm SE$ , where  $n$  is the number of reciprocal edges. SE is calculated by the shot noise  
1222 as  $SE = \sqrt{n}$ .

1223

1224 **Figure S3. Interactions of axon guidance receptors and cues.**

1225 **A.** Image of the 384-well plate and absorbance at 650 nm for the ECIA experiment for selected  
1226 axon guidance-related proteins in Figure 3B.

1227 **B.** ECIA experiment for other guidance-related proteins. *D. melanogaster* Rst is a homodimeric  
1228 protein and serves as a control.

1229

1230 **Figure S4. The ZIG-insulin interactome.**

1231 **A.** Sequence alignment of four ZIGs and the fly ortholog, Impl2. ZIG-2 to -5 carry a disulfide  
1232 unique to all worm ZIGs.

1233 **B.** The ECIA construct design where ZIGs are depicted as bait and insulins as prey, as used in  
1234 the experiment presented in Figure 4B.

1235 **C, D.** Expression of all insulin and ZIG constructs used in the experiment presented in Figure 4B.  
1236 Expression of bait is shown in C and expression of prey in D.

1237 **E.** Kinetic fitting of SPR sensorgrams from Figure 4D with parameters.

1238 **F.** Superposition of three ZIG-4-INS-6 structures solved using three different crystal forms.

- 1239 **G.** The INS-6–ZIG-4 complex is compatible with insulins interacting with the L1 domains +  $\alpha$ CT  
1240 helix in insulin receptors. hIR: human insulin receptor; PDB ID: 3W11.  
1241 **H.** Structure of the active T-like IR<sub>2</sub>-insulin<sub>4</sub> structure from PDB ID: 6PXV. Four insulin-binding  
1242 sites are shown in red, yellow, blue and pink.  
1243 **I, J.** Insulin-bound ZIG-4 would severely clash with dimeric IR, regardless of insulin binding to site  
1244 1 (I), or site 2 (J).  
1245

1246 **Figure S5. Comparison of AlphaFold models of complexes discovered by the ECIA screen**  
1247 **with the structure of human ligand-bound neurotrophin receptor.**

- 1248 **A.** Structure of human neurotrophin receptor, TrkB (domain 5) bound to NT4/5 (PDB: 1HCF).  
1249 **B.** AlphaFold-predicted TRK-1 ectodomain bound to ZK856.6 at a 2:2 stoichiometry.  
1250 **C.** AlphaFold-predicted TRK-1 ectodomain bound to B0416.2 at a 2:2 stoichiometry.  
1251 **D.** PAE (Predicted Aligned Error) plots corresponding to models shown in B. and C. High ipTM  
1252 (interface predicted Template Modelling) scores indicate high-confidence predictions.  
1253 **E.** Kinetic fitting of SPR sensorgrams collected for the binding of B0222.11 to HIR-1, shown in  
1254 Figure 5C.  
1255

1256 **Figure S6. Interfaces observed in AlphaFold models of RIG-5-NLR-1 and RIG-5-PTP-3**  
1257 **complexes.**

- 1258 **A.** The AlphaFold-predicted interface of RIG-5 (ECD) bound to NLR-1 (D6).  
1259 **B.** The AlphaFold-predicted interface of RIG-5 (ECD) bound to PTP-3 (FN4-6). The RIG-5  
1260 residues mutated in the experiment presented in Figure 6H are shown in light cyan in A and B.  
1261

1262 **Figure S7. Binding experiments for NLG-1–NRX-1 complex.**

- 1263 **A.** SPR sensorgrams for soluble NRX-1 LNS6 domain binding to immobilized NLG-1 ECD.  
1264 **B.** Binding isotherm and  $K_D$  for binding shown in A.  
1265 **C.** Size-exclusion chromatography runs for NRX-1 LNS-6 (orange), NLG-1 ECD (green) and the  
1266 mixed sample (black).  
1267

1268 **Table S1. Excel file containing even more data too large to fit in a PDF.**

1269 Ectodomains used in the interactome study by gene, transcript and protein names, sequence,  
1270 domain composition, signal peptide and membrane anchoring predictions. TM: transmembrane.  
1271 Relative expression levels are measured and reported in columns P and Q for bait and prey  
1272 constructs, respectively.  
1273

1274 **Table S2. Excel file containing even more data too large to fit in a PDF.**

- 1275 **A.** Symmetrized z-scores using the MaxEnt method.  
1276 **B.** Asymmetric z-scores using the MaxEnt method.  
1277

1278 **Table S3. Excel file containing even more data too large to fit in a PDF.**

1279 List of interactions observed in the high-throughput ECIA experiment using our new MaxEnt  
1280 method with 2-hour absorbance measurements. Interactions with only one orientation with  $z > 3$   
1281 are labeled pink in column G. For comparison, scoring according to our old method, geometric  
1282 mean of trimmed z-scores ( $\sqrt{(z_1 \times z_2)_{old}}$ ) (Özkan, et al. *Cell*, 2013), are given in H, where a score  
1283 of  $> 20$  was considered significant. Column I reports if the interaction or an orthologous one was

1284 reported before, based on a literature search. Alphafold-multimer (Colabfold version 1.5.2) iPTM  
1285 scores for a subset of interacting pairs are in column J.  
1286

1287 **Table S4. Excel file containing even more data too large to fit in a PDF.**

1288 **A.** Canonical neighbors for every ectodomain tested, protein/sequence names in top row in bold.

1289 **B.** All neighbors for every ectodomain tested, protein/sequence names in top row in bold.  
1290

1291 **Table S5.** Data and refinement statistics for x-ray crystallography of the ZIG-4–INS-6 complex.  
1292

1293 **Table S6. Excel file containing even more data too large to fit in a PDF.**

1294 Experimental details and parameters for all surface plasmon experiments included in the  
1295 manuscript. Biacore chips are purchased from Cytiva. HBSp+: 10 mM HEPES, 150 mM NaCl,  
1296 0.05% Tween-20.  
1297

1298 **Table S7. Excel file containing even more data too large to fit in a PDF.**

1299 185 experimental PPIs based on the number of chemical synapses associated with each  
1300 interaction. Interactions where there was no expression data for one or both of the binding  
1301 partners are labeled N/A. We randomize the neuron connectome as a random control.  
1302

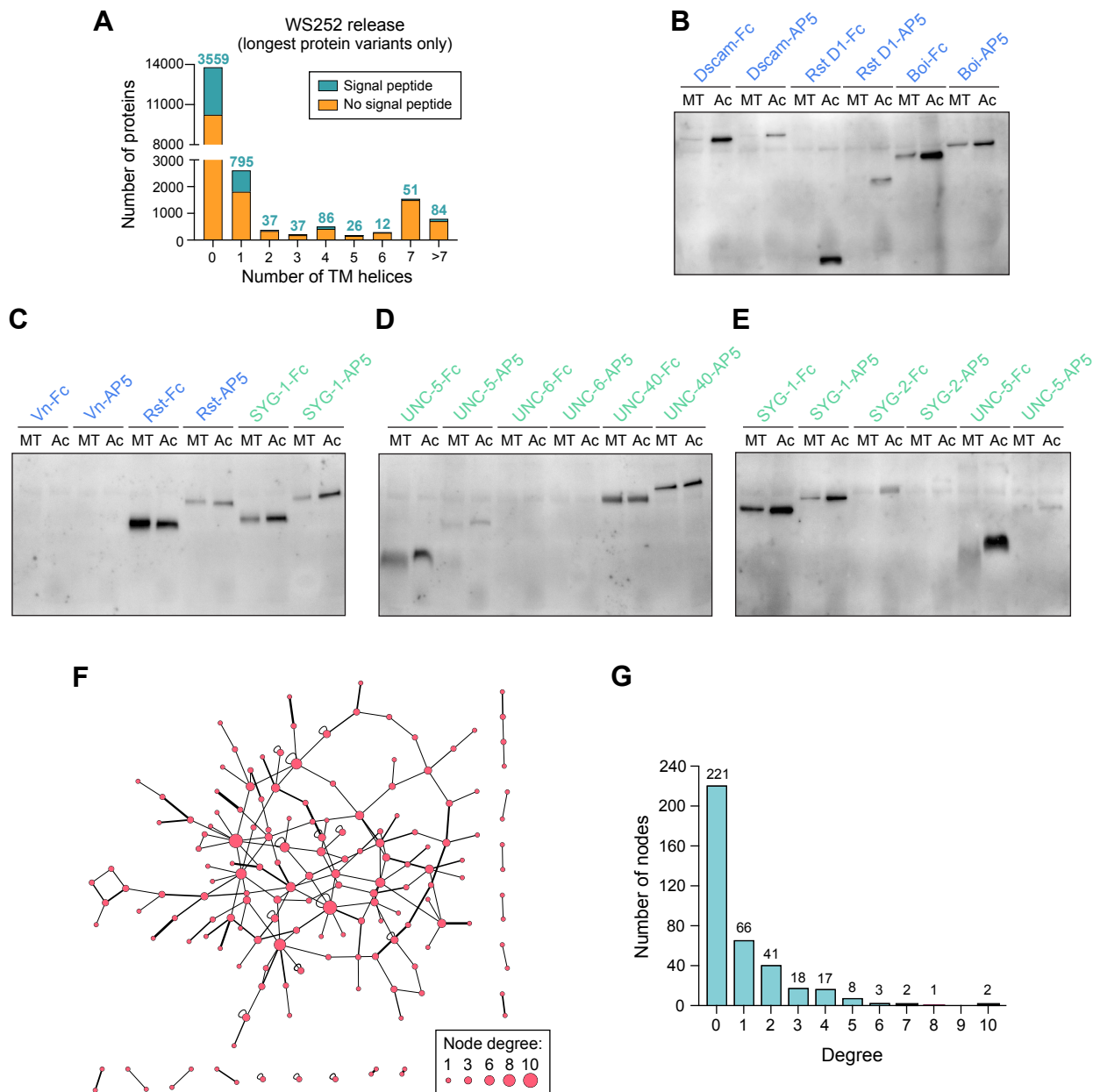


**Figure S1.** Domain collection, protein expression and network analysis.

**A.** Signal peptide and transmembrane helix analysis of the *C. elegans* proteome (WS252 release) shows that 23% of proteins have predicted signal peptides, and 44% of proteins are either membrane-anchored or secreted.

**B-E.** Expression testing of *D. melanogaster* (blue) and *C. elegans* (green) ectodomains in S2 cells using the Metallothionein (MT) and Actin 5C (Ac) promoters. Rst D1 refers to the first immunoglobulin domain of Rst. For MT-driven expression, transiently transfected cells were induced with 0.8 mM CuSO<sub>4</sub> at 16 hours post-transfection. All transfections were collected 88 hours post-transfection for western blotting using a mouse primary anti-His antibody (1:2000) and an Alexa Fluor 488-coupled donkey anti-mouse IgG secondary antibody (1:5000). Overall, the Actin 5C promoter results in higher expression, but not in every case.

**F.** Network of 185 interactions detected with a cutoff of  $z_{\min} > 8.4$  drawn using the organic layout algorithm in Cytoscape, where node size relates to node degree (see the legend), and the edge thickness scales to  $z_{\min}$ .

**G.** The degree distribution of all the interactions depicted in F.



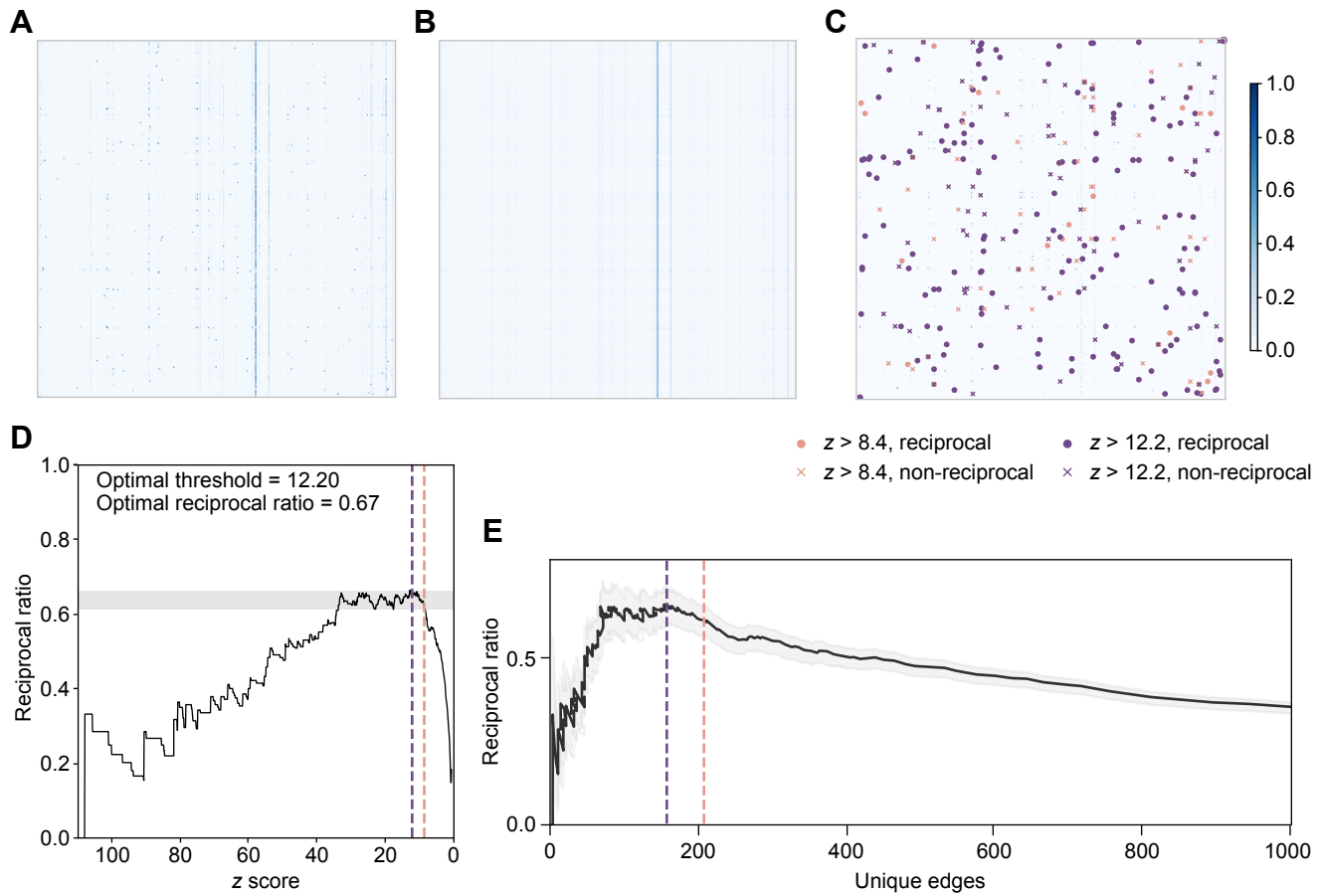


**Figure S2.** MaxEnt model to filter the experimental data.

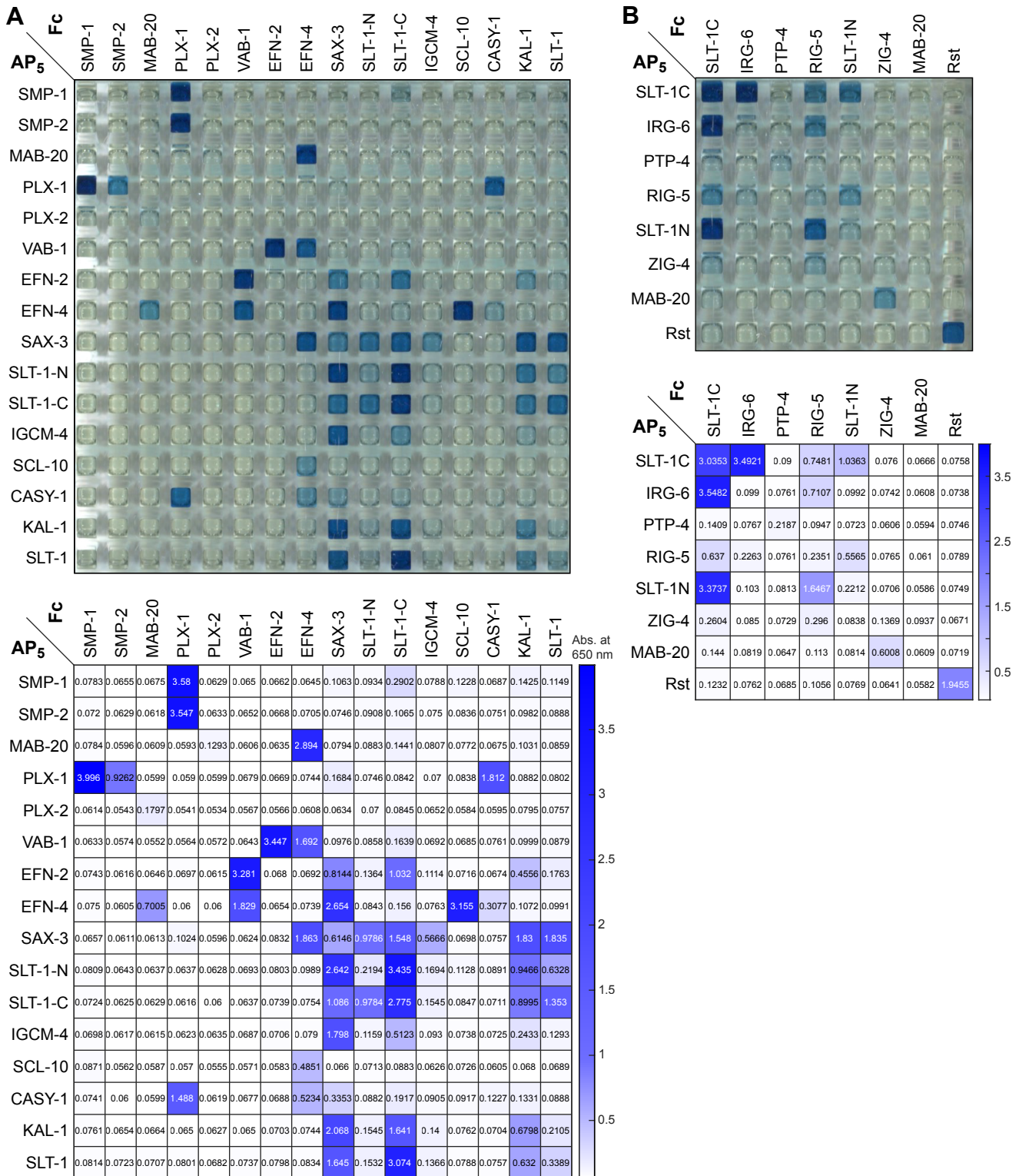
**A.** The normalized experimental data  $A_n$ .

**B.** The mean of the statistical background model  $P$ .

**C.** The difference between  $A_n$  and  $P$ . PPIs with z-score above intermediate (orange) and stringent (purple) thresholds are shown in matrix form. Reciprocal PPIs are marked with a dot (•) and non-reciprocal PPIs are marked with an 'x'.

**D.** The reciprocal ratio of interactions as a function of the chosen threshold of z-scores. The maximum reciprocal ratio is achieved with  $z = 12.2$ .

**E.** The reciprocal ratio as a function of the number of unique edges identified. The shading represents  $n \pm SE$ , where  $n$  is the number of reciprocal edges.  $SE$  is calculated by the shot noise as  $SE = \sqrt{n}$ .



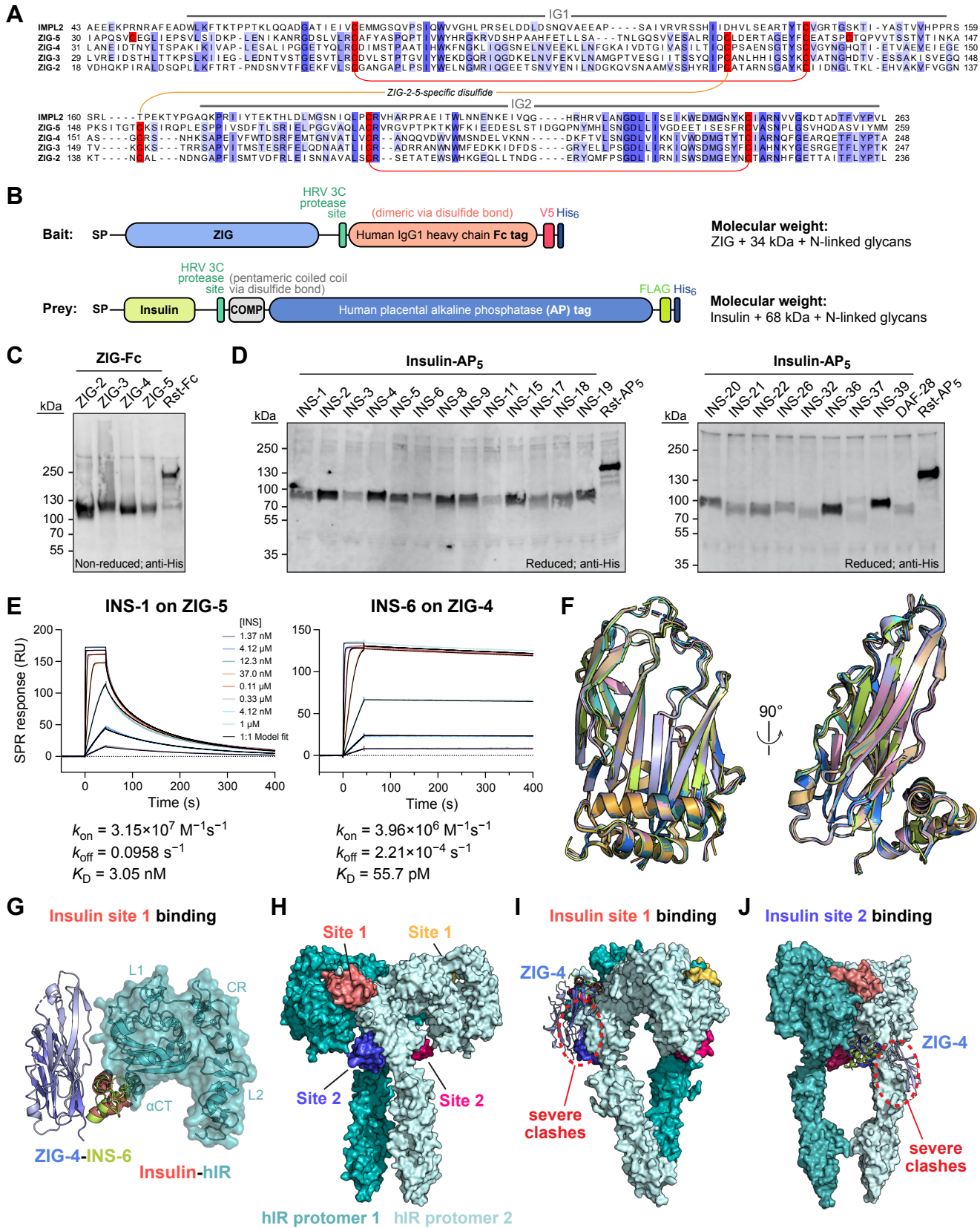


**Figure S4.** The ZIG-insulin interactome.

**A.** Sequence alignment of four ZIGs and the fly ortholog, ImpL2. ZIG-2 to -5 carry a disulfide unique to all worm ZIGs. (continued)

*(continued)*

**B.** The ECIA construct design where ZIGs are depicted as bait and insulins as prey, as used in the experiment presented in Figure 4B.

**C, D.** Expression of all insulin and ZIG constructs used in the experiment presented in Figure 4B. Expression of bait is shown in C and expression of prey in D.

**E.** Kinetic fitting of SPR sensorgrams from Figure 4D with parameters.

**F.** Superposition of three ZIG-4-INS-6 structures solved using three different crystal forms.

**G.** The INS-6-ZIG-4 complex is compatible with insulins interacting with the L1 domains +  $\alpha$ CT helix in insulin receptors. hIR: human insulin receptor; PDB ID: 3W11.

**H.** Structure of the active T-like IR<sub>2</sub>-insulin<sub>4</sub> structure from PDB ID: 6PXV. Four insulin-binding sites are shown in red, yellow, blue and pink.

**I, J.** Insulin-bound ZIG-4 would severely clash with dimeric IR, regardless of insulin binding to site 1 (I), or site 2 (J).



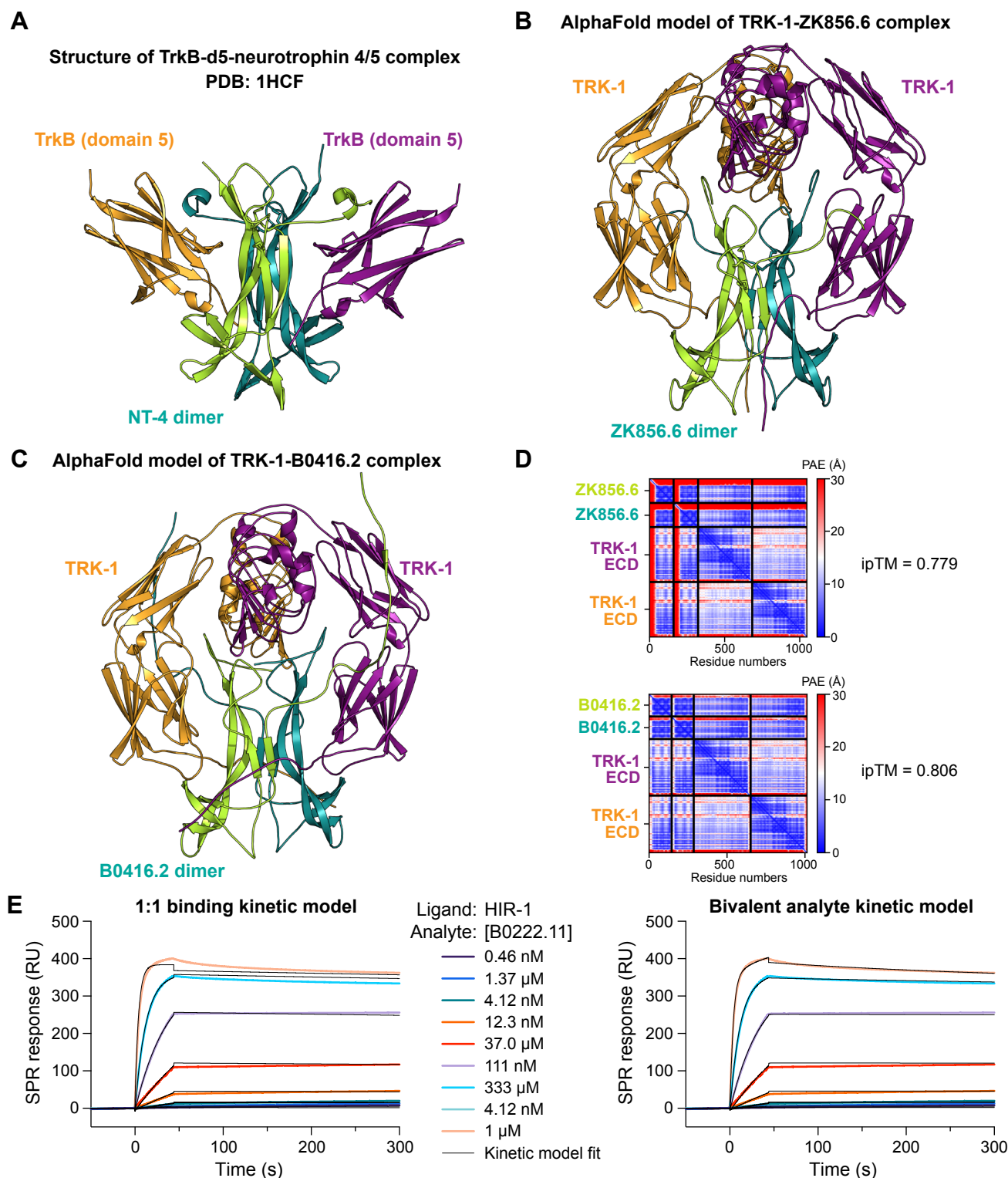


**Figure S5.** Comparison of AlphaFold models of complexes discovered by the ECIA screen with the structure of human ligand-bound neurotrophin receptor.

**A.** Structure of human neurotrophin receptor, TrkB (domain 5) bound to NT4/5 (PDB: 1HCF).

**B.** AlphaFold-predicted TRK-1 ectodomain bound to ZK856.6 at a 2:2 stoichiometry.

**C.** AlphaFold-predicted TRK-1 ectodomain bound to B0416.2 at a 2:2 stoichiometry.

**D.** PAE (Predicted Aligned Error) plots corresponding to models shown in B. and C. High ipTM (interface predicted Template Modelling) scores indicate high-confidence predictions.

**E.** Kinetic fitting of SPR sensorgrams collected for the binding of B0222.11 to HIR-1, shown in Figure 5C.

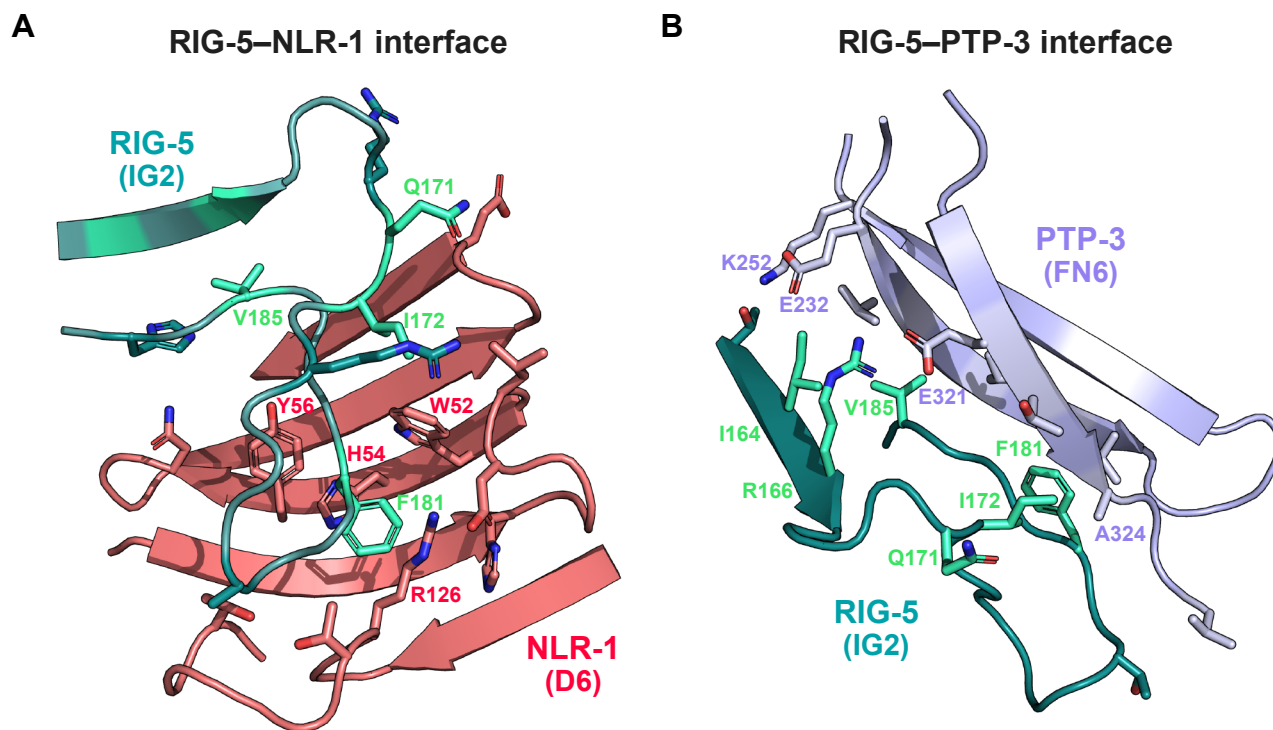


**Figure S6.** Interfaces observed in AlphaFold models of RIG-5-NLR-1 and RIG-5-PTP-3 complexes.

**A.** The AlphaFold-predicted interface of RIG-5 (ECD) bound to NLR-1 (D6).

**B.** The AlphaFold-predicted interface of RIG-5 (ECD) bound to PTP-3 (FN4-6). The RIG-5 residues mutated in the experiment presented in Figure 6H are shown in light cyan in A and B.



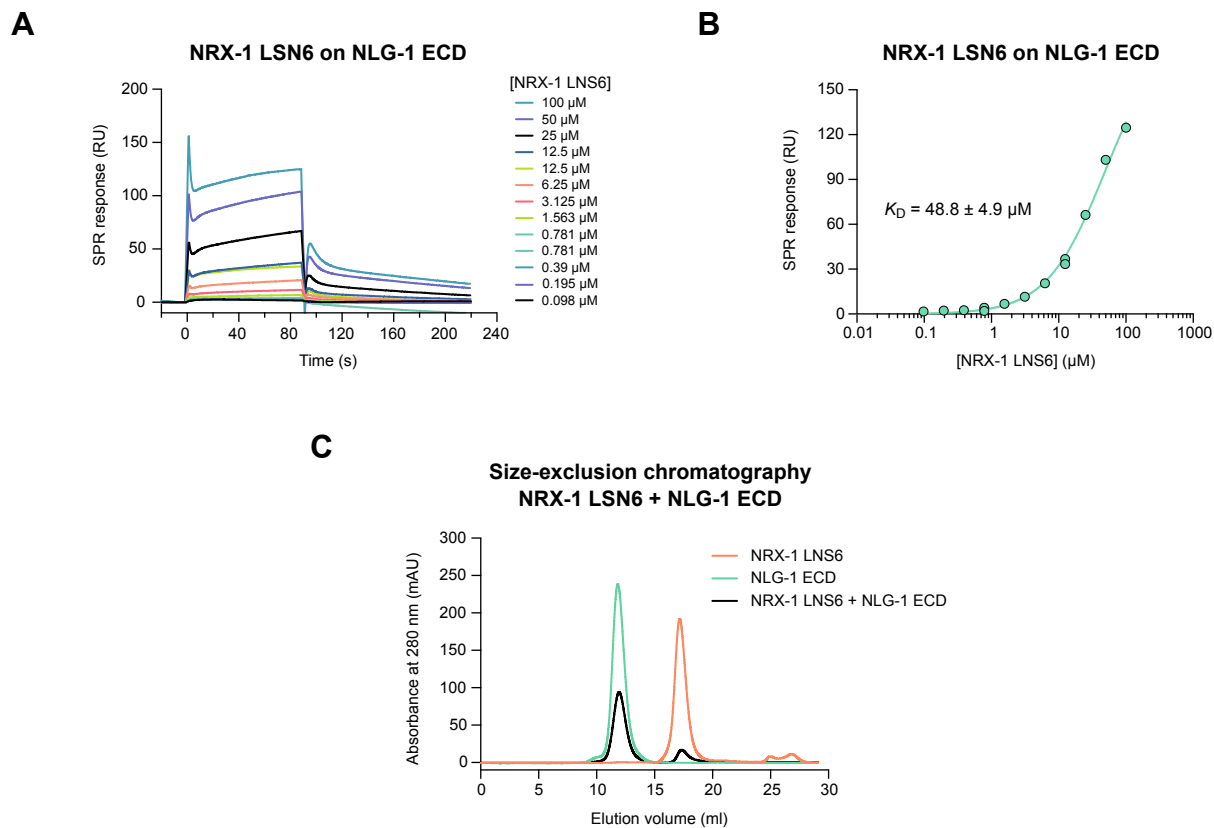


**Figure S7.** Binding experiments for NLG-1–NRX-1 complex.

**A.** SPR sensorgrams for soluble NRX-1 LSN6 domain binding to immobilized NLG-1 ECD.

**B.** Binding isotherm and  $K_D$  for binding shown in A.

**C.** Size-exclusion chromatography runs for NRX-1 LSN-6 (orange), NLG-1 ECD (green) and the mixed sample (black).

**Table S5.** Data and refinement statistics for x-ray crystallography of the ZIG-4–INS-6 complex.

	<b>Tetragonal form</b>	<b>C-centered monoclinic</b>	<b>Primitive monoclinic</b>
<b>Data Collection</b>			
Beamline	APS 24-ID-E	APS 24-ID-E	APS 24-ID-E
Space Group	$P4_22_12$	$C2$	$P2_1$
<i>Cell Dimensions</i>			
$a, b, c$ (Å)	74.528, 74.528, 107.058	166.430, 56.654, 73.685	73.839, 55.739, 149.945
$\alpha, \beta, \gamma$ (°)	90, 90, 90	90, 113.247, 90	90, 93.775, 90
Resolution (Å)*	200-1.30 (1.38-1.30)	200-2.30 (2.44-2.30)	200-2.35 (2.49-2.35)
$R_{\text{sym}}$ (%)	4.6 (120.1)	7.1 (113.1)	6.2 (124.8)
$\langle I \rangle / \langle \sigma(I) \rangle$	24.0 (1.78)	9.7 (1.1)	10.7 (0.9)
$CC_{1/2}$	0.999 (0.742)	0.998 (0.652)	0.998 (0.463)
Completeness (%)	99.8 (99.4)	98.4 (96.7)	97.9 (97.1)
Redundancy	12.8 (12.2)	3.4 (3.3)	3.1 (3.1)
<b>Refinement</b>			
Resolution (Å)*	50-1.30 (1.32-1.30)	53.13-2.30 (2.38-2.30)	74.81-2.35 (2.60-2.50)
Reflections	73,784	27,969	50,096
$R_{\text{cryst}}$ (%)	14.47 (27.19)	21.52 (43.52)	19.66 (38.72)
$R_{\text{free}}$ (%)**	16.89 (31.58)	25.18 (47.21)	23.98 (44.33)
<i>Number of atoms</i>			
Protein	2,128	3,878	7,755
Ligand/Glycans	11	0	0
Water	305	7	39
<i>Average B-factors (Å<sup>2</sup>)</i>			
All	24.8	76.2	83.1
Protein	23.0	76.3	83.2
Ligand	36.3	N/A	N/A
Solvent	37.0	60.2	57.5
<i>R.m.s. deviations from ideality</i>			
Bond Lengths (Å)	0.012	0.003	0.008
Bond Angles (°)	1.291	0.631	1.002
<i>Ramachandran plot</i>			
Favored (%)	98.41	96.67	97.24
Outliers (%)	0.40	0.00	0.00
Rotamer Outliers (%)	0.43	0.48	0.39
All-atom Clashscore <sup>‡</sup>	3.34	3.31	3.91

\* The values in parentheses are for reflections in the highest resolution bin.

\*\* 5% of reflections (3,747) for tetragonal crystals, 5% of reflections (1,373) for C-centered monoclinic crystals, and 4% of reflections (1,977) for primitive monoclinic crystals were not used during refinement for cross validation purposes.

‡ Clashscores were calculated by *phenix.refine* (Phenix version 1.21).

N/A: Not applicable.